UNIVERSIDADE
BEIRA INTERIOR

Characterisation of Monodisperse Regimes of a Droplet Stream Generator

(Versão Final Após Defesa)

João Carlos Canhoto Cardoso

Dissertação para obtenção do Grau de Mestre em
Engenharia Aeronáutica
(Mestrado Integrado)

Orientador: Prof. Doutor André Resende Rodrigues da Silva

Covilhã, maio de 2021

Agradecimentos

Primeiramente, quero agradecer ao Professor André Silva por me ter proposto este trabalho e por me ter orientado ao longo de todo o processo de desenvolvimento desta dissertação.

Gostaria também de agradecer a oportunidade de pertencer ao AEROG - Aeronautics and Astronautics Research Center. Este trabalho não poderia ser realizado sem os recursos fornecidos por este laboratório.

Gostaria de agradecer aos membros do laboratório que, de uma maneira ou de outra, me ajudaram durante o percursso de realização da dissertação. Gostaria de agradecer especialmente ao Daniel Vasconcelos e à Daniela Ribeiro por toda a ajuda que me deram e pela imensa disponibilidade e paciência que sempre tiveram.

Um obrigado ao técnico de laboratório, o senhor Rui Manuel Tomé Paulo, que me ajudou na construção da instalação experimental.

Gostaria ainda de agradecer aos meus melhores amigos, que tive a sorte de conhecer durante o meu percurso académico. Sem eles, todo o meu percurso não tinha o mesmo valor e significado. Ficarei para sempre grato por ter tido a sorte de os encontrar.

Por fim, gostaria de agradecer à minha familia, à minha irmã Teresa, ao meu pai Manuel e à minha mãe Susana. Em todos os momentos do meu percurso académico e de desenvolvimento desta dissertação me deram um apoio incondicional e força para continuar.

Resumo

O interesse em estudar fenómenos relacionados com as gotas tem vindo a aumentar nas últimas décadas. Na indústria de equipamentos de ejeção de fluidos, um grande problema é minimizar o diâmetro das gotas e ejetá-las de forma controlada utilizando um dispositivo de baixo custo. A geração de micro-gotas ganhou popularidade pelas suas múltiplas aplicações, como biotecnologia, engenharia de fabricação e ejeção de combustível. Tendo tudo isto em conta, um novo gerador de gotas contínuas, de baixo custo, foi projetado e fabricado. PLA foi o material usado para fabricar a estrutura do gerador de gotas dado que é um material de impressão 3D, o que permite minimizar o custo do dispositivo. Esta estrutura tem três componentes separados: tampa da célula piezoelétrica, câmara de fluido e suporte do pinhole. A fim de simplificar o mecanismo de perturbação, foi decidido que as ondas de perturbação devem ser aplicadas diretamente no fluido. Para conseguir isso, uma célula piezoelétrica foi colocada acima da câmara de fluido. O ”nozzle” utilizado é um pinhole óptico redondo de alta precisão, feito de de aço inoxidável e com três tamanhos diferentes: $100\ \mu m$, $150\ \mu m$ e $200\ \mu m$. As propriedades do jato (diâmetro da gota, velocidade da gota e distância entre gotas) foram medidas de para diferentes propriedades (frequência da célula piezoelétrica, pressão de fluído e tamanho do ”nozzle”). O presente trabalho estudou as características do spray para três fluidos diferentes (àgua, jet fuel e mistura de biocombustível) e diferentes regimes monodispersos foram encontrados. Uma caracterização destes parametros é apresentada e discutida com detalhe. Verificou-se que o intervalo do diâmetro das gotas para um ”nozzle” com tamanho de $200\ \mu m$, que pode ser usado para todos os três fluidos, é de $401\ \mu m$ até $472\ \mu m$ e o intervalo de velocidade é de $1,24\ m/s$ até $2,48\ m/s$, enquanto que para um ”nozzle” com um tamanho de $150\ \mu m$, a gama de diâmetros que pode ser obtido é de $287\ \mu m$ até $340\ \mu m$ e um intervalo de velocidade de $2,04\ m/s$ até $4,38\ m/s$, para os três fluidos. Para um tamanho de pinhole de $100\ \mu m$, o intervalo de diâmetros das gotas para todos os três fluidos é de $206\ \mu m$ a $258\ \mu m$ e o intervalo de velocidade é $2,36\ m/s$ a $5,99\ m/s$. Verificou-se que, tanto o diâmetro da gota como o espaçamento, diminuem com o aumento da fluxo da entrada e frequência, e a propriedade mais importante na formação do jato é o tamanho do ”nozzle”. A velocidade do jato é muito influenciada pela velocidade do fluxo e pelo tamanho do ”nozzle”. Quando comparados, os três fluidos comportam-se de uma forma diferente, resultando em diferentes diâmetro de gotas e velocidade do jato. Isto pode ser explicado pelas propriedades dos fluidos, onde a mistura de biocombustível apresenta maior viscosidade do que os outros dois fluídos.

Palavras-chave

Jato de Gotas Contínuas, Regime Monodisperso, Gerador de Gotas Piezoelétrcio, Formação de Jato, Rayleigh Breakup, Jet Fuel e Biocombustível.

Abstract

The interest in studying droplet related phenomena has been increasing over the last decades. In the fluid dispensing equipment industry, a major problem is to minimise droplet diameter and to eject droplets in a controlled manner with a low-cost device. Micro-droplet generation has gained its popularity for its multiple applications, such as biotechnology, manufacturing engineering, and fuel dispensing. Taking all this into account, a new low-cost droplet stream generator was designed and fabricated. The material used to manufacture the stream droplet generator structure was PLA, since it is a 3D printable material, which allowed to minimise the device cost. This structure has three separated components: lid, fluid chamber, and pinhole holder. In order to simplify the disturbance mechanism, it was decided that the disruption waves should be applied directly to the fluid. To achieve that, a piezoelectric cell that vibrates through the variation of waveform parameters was placed above the liquid chamber, creating disturbances directly onto the liquid surface in a parallel direction, making this device a push mode generator. The interchangeable nozzle used was a round stainless-steel high precision optical pinhole with three different sizes: $100\ \mu m$, $150\ \mu m$, and $200\ \mu m$. Jet attribute properties (droplet diameter, droplet velocity, and distance between droplets) were measured as the different conditions changed (piezoelectric diaphragm frequency, outlet pressure, and nozzle size). The present work studied the spray characteristics for water, jet fuel and a jet fuel and biofuel mixture, and different monodisperse regimes were found. A full characterisation of them is presented and discussed in detail. It was found that the range of droplet diameter for a pinhole size of $200\ \mu m$ that can be used for all three fluids is $401\ \mu m$ to $472\ \mu m$ and a range of velocity of $1.24\ m/s$ to $2.48 m/s$, while for a pinhole size of $150\ \mu m$ the droplet diameter range that can be obtained is $287\ \mu m$ to $340\ \mu m$ and a range of velocity of $2.04\ m/s$ to $4.38\ m/s$ for all three fluids. For a pinhole size of $100\ \mu m$ the droplet diameter range for all three fluids is $206\ \mu m$ to $258\ \mu m$ and the velocity range is $2.36\ m/s$ to $5.99\ m/s$. It was found that both droplet diameter and spacing decrease with the increase of inlet flow rate and frequency, and the most important property in the jet formation is the nozzle size. The jet velocity is also highly influenced by the flow rate and nozzle size. When compared, the three fluids behave in a different manner, resulting in different droplet diameter and velocity values. This can be explained by the fluids properties, where the mixture of jet fuel and biofuel presents higher viscosity than the other two fluids.

Keywords

Droplet Stream Jet, Monodisperse Regime, Piezoelectric Droplet Generator, Rayleigh Breakup, Jet Formation, Jet Fuel and Biofuel.

Contents

List of Figures

List of Tables

Nomenclature

a	Length scale
Bo	Bond number
d	Nozzle diameter
D	Droplet diameter
f	Frequency
I_0	Modified bessel function
I_1	Modified bessel function
k	Dimensional wave number
ka	Dimensionless wave number
L	Droplet centroid distance
Oh	Ohnesorge number
R	Interface radius of curvature
Re	Reynolds number
s	Space between droplets
U	Jet velocity
W	Wavelength
We	Weber number
We_0	Weber critical number

Greek Symbols

ζ	Wave amplitude
λ	Continuous jet length
μ	Viscosity
ρ	Density
σ	Surface tension
ω	Instability growth
ω_i	Oscillation frequency
ω_r	Growth rate

Subscripts

d	Droplet
j	Jet

Acronyms List

CAD	Computer-aided design
$CATIA$	Computer-aided three-dimensional interactive application
DOD	Drop-on-demand
fps	Frames per second
HVO	Hydroprocessed vegetable oil
JF	Jet fuel
$MATLAB$	Matrix algorithm
MD	Monodisperse regime
MD^*	Multiple monodisperse regimes
PHB	Pinhole holder base
PHL	Pinhole holder lid
PLA	Polylactic acid

Chapter 1

Introduction

This chapter starts by explaining the reasons that motivated the realisation of the present work. Then, a brief literature review is presented and different topics are detailed, such as the instability of liquid jets, plain orifice atomisers, devices for controlled droplet formation, and piezoelectric droplet generators. After, the objectives proposed for this work are presented. Finally, the organisation of this dissertation is detailed.

1.1 Motivation

This dissertation reports an optimisation and characterisation of a droplet generator. Science in general and engineering in particular are all about creating and optimising. This dissertation consists in optimising a previous work, in order to improve some of the micro-droplet generator technical issues. Thus, those who follow this work can have a fully functional tool that can be used in several different studies.

The interest on devices that produce small droplets with controlled size was initially developed to improve the resolution of ink-jet printing. Since then, the interest of this kind of devices has been expanded to other areas such as biotechnology and manufacturing engineering, as well as for combustion applications such as research on the impact of droplets on solid surfaces or liquid films and mechanical droplet-droplet interaction. For the combustion application, it is important that for the droplets to be as small as possible and with a controlled size, in order to optimise the combustion process and possible reducing the gas emissions in different sectors, like aviation. Thus, it is important to study the behaviour of atomised fluids with this type of devices.

In line to the problematic of gas emissions in the aviation sector, the use of biofuels are seen as one of the alternatives for the typical aviation jet fuel. Thus, it is important to study the differences between those fluids in an attempt to introduce them in internal combustion engines.

1.2 Literature Review

The study of droplet formation dates back over a century, as well as its multiple utilities for engineering and investigation purposes. The formation of droplets by slow emission of a liquid from a nozzle forms a pendant droplet that grows slowly, and when the gravity forces exceed the surface tension, a droplet is formed. This mechanism can be associated as drip-

ping and usually produces large droplets with low production rates. When the liquid flow rate is progressively increased, increasing the liquid velocity, a continuous jet is formed and droplets are generated by the spontaneous breakup of the jet. This process of droplet formation is referred to as Rayleigh breakup. When the liquid velocity is further increased, the aerodynamic effects can no longer be neglected and can accelerate the breakup process. At still higher velocities, we enter the atomisation regime characterised by the appearance of a spray [1].

In the following subsections, different regimes of breakup in the disintegration of a liquid jet will be presented and explained, with particular emphasis to the Rayleigh breakup. Then, the governing parameters for jet formation and plain orifice atomisers will be issued. Finally, some droplet stream generators and piezoelectric generators present in the literature will be shown.

1.2.1 Instability of Liquid Jets

When a liquid jet emanates from a nozzle into an ambient gas, the liquid/gas interface is deformed and the surface tension forces may tend to bring it back to the equilibrium shape, rising disturbances on the jet surface and, under certain conditions, amplifying the disturbances and disintegrating the liquid into droplets. These disturbances can be in the form of surface displacement, pressure or velocity fluctuations within the supply system or on the jet surface, as well as fluctuations in liquid properties such as temperature, viscosity, or surface tension. Pressure disturbances can be due to the application of a sound wave on the jet. Surface disturbances also can occur by employing a piezoelectric transducer at the nozzle which contracts and expands periodically by applying a periodic voltage on it, while velocity disturbances can be applied by using an oscillating flow, and temperature disturbances can be introduced by applying periodic heating on a jet. [2]

During the jet formation process, as the disturbed interface tends to move to its equilibrium shape, a wave like the one in figure 1.1 appears, where W represents the wavelength, a represents the jet radius, R_1 and R_2 are the principal radii of curvature of the interface, and ζ represents the wave amplitude. The properties of the jets of most interest are the jet continuous length and the droplet size. The first can provide a measure of growth rate of the disturbance and the second is a measure of the wave number of the most unstable disturbance.

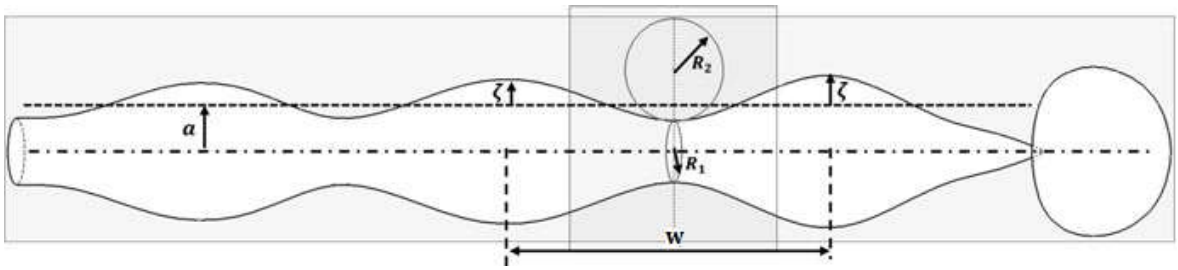

Figure 1.1: Schematic of an unstable jet [2].

The jet disintegration phenomenon has been studied for more than 100 years. One of the earliest investigations were performed by Savart [3], where he showed the behaviour of the continuous jet part length with the velocity and jet diameter. If the jet diameter is kept constant, the length of the continuous part of the jet is directly proportional to the jet velocity, while for a constant jet velocity, the length of a jet is directly proportional to the jet diameter. After that, Plateu [4] showed that a cylindrical column of liquid is unstable if its length exceeds its perimeter. These two analyses helped Rayleigh [5] to perform a mathematical analysis where, assuming that the liquid was inviscid, he predicted the growth rate of a given axisymmetric surface disturbance for the maximum instability.

With this analysis, it is possible to predict the instability growth rate by means of the dimensionless wave number, as seen in equation 1.1, where k is the wave number, ka is the dimensionless wave number, σ represents the fluid surface tension, ρ represents the fluid density, the a is the jet radius, I_0 and I_1 are Bessel functions, and $\omega = \omega_r + i\omega_i$, with ω_r being the growth rate and ω_i being the oscillation frequency.

$$\omega^2 = \frac{\sigma k}{\rho a^2}(1 - k^2a^2)\frac{I_1(ka)}{I_0(ka)} \quad \textbf{(1.1)}$$

If the real part of the growth rate is positive, the disturbances grow exponentially in time. The ratio of the modified Bessel functions is positive for all conditions $(I_1/I_0) > 0$. This means that ω is a real positive as long as $ka < 1$ and the capillary pinching dominates over the restoring capillary force. This leads to the conclusion that the jet should be unstable for wave numbers between 0 and 1. In other words, any disturbance with a wavelength larger than the diameter of the jet, makes the jet unstable. When $ka > 1$, the disturbances applied to the jet surface are stable and the restoring forces are sufficiently large to overcome the capillary pinching.

Further, Rayleigh [5] obtained an expression for the resulting droplet size to a maximum instability, shown in equation 1.2, where D is the droplet diameter and d is the jet diameter, that is frequently considered the same as the nozzle diameter. Therefore, the average droplet size for the Rayleigh breakup mechanism is nearly twice the diameter of undisturbed jet.

$$D = 1.89d \quad \textbf{(1.2)}$$

A new diameter value for the droplets generated with this mechanism was later obtained by Tyler [6] in his experimental studies, seen in equation 1.3, where he assumed the volume of the spherical droplets formed by the disintegration of the jet is equal to the volume of a cylinder with a diameter equal to the undisturbed jet diameter and considered the wavelength to be equal to the most rapidly growing disturbance. Similar to Rayleigh, Tyler found that

this value can be obtained for maximum instability.

$$D = 1.92d \quad (1.3)$$

Weber [7] extended Rayleigh analysis to include viscous liquids. He found that the effect of the liquid viscosity is to shift the fastest growing waves to longer wavelengths and to slow down their growth rate, without, however, altering the value of the minimum wave number that makes the jet unstable. This means that the viscosity damps the instability growth, as it can be seen in figure 1.2. The maximum growth rate and the corresponding wave number decrease with the increase of the Ohnesorge number, leading to the conclusion that the perturbations in fluids with high viscosity have smaller growth rate than in fluids with small viscosity.

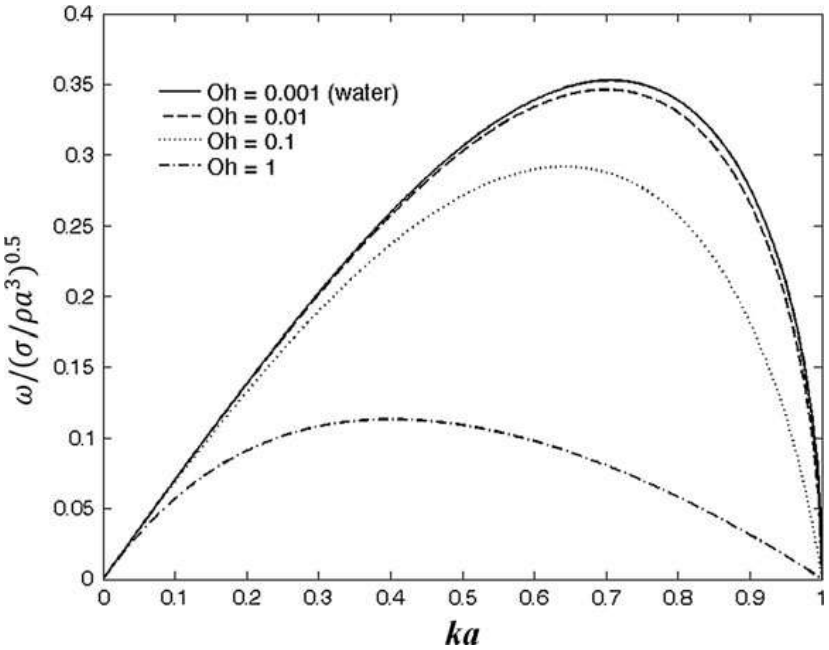

Figure 1.2: Growth rate of small capillary perturbations of viscous jets instability in terms of the wave number for different fluids [2].

Later, Weber [7] examined the effect of air resistance in the jet formation process and found that the air friction shortens both the minimum wavelength and the optimum wavelength for droplet formation.

Haenlein [8] presented experimental evidence supporting Weber theory and identified four different regimes of breakup in the disintegration of a liquid jet. The first regime is the droplet formation without the influence of air, that is to say, the mechanism studied by Rayleigh. The second regime is characterised by a droplet formation with air influence. In this regime, the aerodynamic forces of the surrounding air are no longer negligible. In the third regime, the droplet formation is obtained due to the waviness of the jet and it is associated with an increase in the aerodynamic forces. The last regime is the complete disintegration of the jet.

After that, other authors tried to clarify the Haenlein regime classification in order to get a more practical identification of the phenomena. Ohnesorge [9] proposed a criterion for classifying jet disintegration. He showed that the jet breakup mechanism could be divided into three regions on a graph of Ohnesorge Number versus Reynolds Number, similar to the one in figure 1.3. The first regime represents the Rayleigh mechanism of breakup. In the second regime, at intermediate Reynolds number, the breakup of the jet occurs by jet oscillations with respect to the axis, and a wide range of droplet size is formed.In the third regime, at high Reynolds numbers, the atomisation is completed.

More recently, Reitz [10] attempted to resolve some of the uncertainties surrounding the Ohnesorge chart. As seen in figure 1.3, four regimes of breakup are encountered as the liquid injection velocity progressively increases. The first regime corresponds to a Rayleigh jet breakup. In the second regime, the wind-induced breakup, the surface tension is now augmented by the relative velocity between the jet and ambient gas and the droplets diameter are about the same as the jet diameter. After that, we have the second wind-induced breakup regime. In this regime, droplets are produced by the unstable growth of short-wavelength surface waves on the jet surface caused by the relative motion of the jet and the ambient gas. The average droplet diameters are much smaller than the jet diameter. The last regime is atomisation, where the jet disrupts completely at the nozzle exit. Average droplet diameters are much lower than the jet diameter.

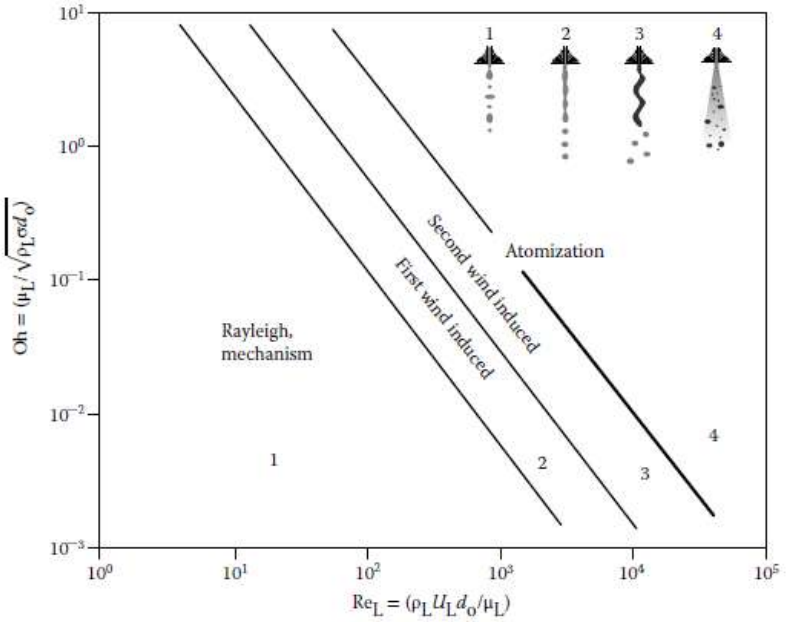

Figure 1.3: Classification of modes of desintegration by Reitz [10].

1.2.2 Governing Parameters

Several studies were performed prior to this study, where, in order to characterise the jet formation, it was necessary to consider different dimensionless numbers. The firs relevant dimensionless number is the Reynolds number, shown in equation 1.4, where the ρ is the

fluid density, U is the jet mean velocity, a is the length scale (e.g. droplet diameter or nozzle diameter) and the μ is the fluid dynamic viscosity. This number represents the ratio between the inertial forces and viscous forces.

$$Re = \frac{\rho U a}{\mu} \quad (1.4)$$

Another relevant dimensionless number is the Weber number, shown in equation 1.5, where σ is the liquid surface tension. The Weber number represents the ratio between the inertial and surface tension forces.

$$We = \frac{\rho U^2 a}{\sigma} \quad (1.5)$$

Combining the previous two numbers in order to eliminate the velocity, results in the Ohnesorge number, presented in equation 1.6. Ohnesorge number represents the influence of the fluid properties. Low Ohnesorge numbers represent either a low viscosity or a high surface tension.

$$Oh = \frac{\sqrt{We}}{Re} = \frac{\mu}{\sqrt{\rho \sigma a}} \quad (1.6)$$

When the gravitational effects are important, the ratio of the gravitational forces to surface tension forces is represented by the Bond number, defined as:

$$Bo = \frac{\rho g a^2}{\sigma} \quad (1.7)$$

1.2.3 Plain Orifice Atomisers

There are several basic processes associated with methods of atomisation. One of the simplest ones is the disintegration of a liquid jet issuing from a circular orifice. These kinds of atomisers are called plain orifice atomisers, where a simple circular orifice is used with the objective of injecting liquid into the surrounding air. Utilising small orifices leads to a finest atomisation, however, the orifice size reduction is limited by the presence of some undesirable particles that can clog the nozzle and smaller orifices tend to clog more than larger ones.

They are the most commonly used atomisers due to their simplicity and ease of manufacture. There are many applications for this type of atomisers, including industrial spraying, inkjet printers and combustion applications such as: diesel engines, rocket engines, and ramjets.

The performance of any type of atomiser depends on its size and geometry, as well as the ambient conditions and the liquid physical properties. The flow and spray characteristics of most atomisers are strongly influenced by the liquid properties: surface tension, density and viscosity. An increase in the viscosity lowers the Reynolds number and also hinders the development of any natural disturbances in the jet, delaying the disintegration and increasing the size of the droplets. With this kind of atomisers, an increase in ambient gas density leads to a wider spray angle. This can be explained by the increase in aerodynamic drag on the droplets, created by an increase in gas density, which tends to produce a greater deceleration in the axial direction than in the radial direction. As stated before, the fluid and air physical properties influence the atomisation process, however, for plain-orifice pressure nozzles specifically, the orifice diameter is the most important factor for atomisation and has great influence on the jet velocity and diameter [11].

1.2.4 Droplet Stream Generators

The essential feature of these generators is that the size of the droplets and the spacing between them can be accurately controlled, obtaining a monodisperse regime. The physical principle mostly used behind these devices operation is a Rayleigh breakup, which already was expalined in section 1.2.1. These devices are important tools for application such as mechanical droplet-droplet interactions, impact of droplets on solid surfaces or liquid films, droplet evaporation, and validation of particle sizing techniques.

1.2.4.1 Range of Operation Parameters

The production of droplets utilising these kind of devices relies on the growth of deformation of laminar-type liquid jets. The first requisite for the application of this technique is that a liquid emerging from a nozzle is formed. In order to achieve that, a certain Weber number, with the nozzle diameter as length scale, of the liquid flow is needed. Walzel [12] derived a critical Weber number (We_0) for which the droplet generation transitions from dripping mode to jetting, as:

$$We > We_0 = 14.5Oh^{0.08} \quad (1.8)$$

The previous value gives the information of when stream jet formation will happen, however, does not provide a range of suitable frequencies for producing monodisperse droplets. Schneider and Hendricks [13] empirically specified a range of suitable dimensionless wave numbers to a monodisperse droplet formation as $0.45 \leq ka \leq 0.95$. On other hand, Breen et al.

[14] found a range of $0.3 \leq ka \leq 0.9$. The actual range for monodisperse drop formation may depend on the nozzle hole profile and shape, and can be found with the following equation:

$$0.3 \leq ka = \frac{\pi}{\sqrt{We}} \sqrt{\frac{\rho d^3}{\sigma}} f \leq 0.9 \quad \textbf{(1.9)}$$

The equation 1.10 can be rewritten as:

$$0.3 \leq ka = \frac{\pi f d}{U} \leq 0.9 \quad \textbf{(1.10)}$$

In this equation, it is possible to understand that the range of dimensionless wave numbers depends on the jet diameter (usually considered to be the same as the nozzle), jet velocity and the disturbance frequency (f in equation 1.10).

1.2.4.2 Devices for Controlled Droplet Formation

The devices used to obtain controlled droplet formation can be divided into two categories. First are the devices that use capillary tubes to produce the liquid jets and the vibration generated around these tubes control the jet break-up. One of the first devices working using this principle was the one developed by Dimmock [15]. Schneider and Hendricks [13] reported another device that vibrates the capillary tube in its axial direction with a piezoelectric transducer, generating a controlled stream jet formation. The further devices developed by Lindbald and Schneider [16] and Schneider et al. [17], included a mechanism where the droplets were electrically charged, enabling the user to deflect a single droplet from the jet using a plate capacitor. This feature is of particular interest for droplet impact studies, since the droplet diameter is small and easy to control.

The second type of devices generates liquid jets using a thin orifice nozzle with nozzle holes. This kind of device can be included in the category of plain orifice atomisers, explained previously. Berlung and Liu [18] developed a droplet generator that vibrates an orifice plate with a single nozzle hole, using a piezoelectric vibrator, that is mounted directly around the nozzle plate, showed in figure 1.4. This droplet generator uses a signal generator for exciting the piezoelectric vibrator and a syringe pump for adjusting the liquid flow rate. This device is not suitable for research with combustion droplets because the piezoelectric ring is mounted at the orifice of the droplet generator, not allowing the droplet generator to be exposed to a hot environment. Also, it is not recommended for investigations with collisions of droplets pairs, since the required spacing of the droplet generator leads to long traveling distances of the droplets to the point of impact. Another droplet generator that uses an orifice plate was developed by Frohn et al. [19], which introduces the vibrations directly into the liquid,

making this device more flexible and easy to use on different applications.

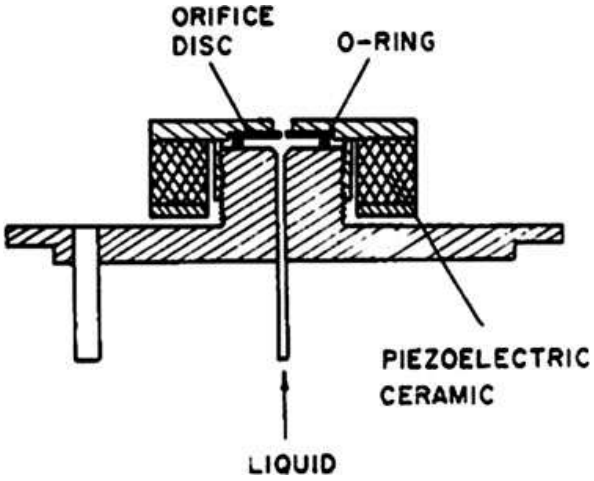

Figure 1.4: Sketch of the vibrating orifice generator by Berlung and Liu [18].

A variation of the single-hole orifice type of devices described above are the multi-hole orifice devices. Breen et al. [14] developed a shower-head monodisperse spray generator that allows large liquid flow rates. The working principle that this device uses is the same of the single-hole droplet stream generators applied to a nozzle plate with a very large numbers of nozzle holes, and uses a single piezoceramic vibrator to generate monodisperse droplets from more than 600 liquid jets. Another droplet generator that uses a multi-hole orifice was developed by Dabora [20]. He proposed to use the principle of liquid jet formation by capillary tubes using more than one capillary needle in the nozzle plate of the generator. The vibrations that enforce the monodisperse droplets were applied with a loudspeaker and it produced droplet sizes between $290\ \mu m$ and $950\ \mu m$.

1.2.5 Piezoelectric Droplet Generators

As stated before, in order to generate monosized and monodisperse droplets in a controlled manner, it is necessary to employ an artificial disturbance. These disturbances can be generated in multiple ways, such as surface displacement, pressure or velocity fluctuations in the supply system or on the jet surface, as well as fluctuations in liquid properties such as temperature, viscosity, or surface tension coefficient. With that in mind, different types of generators were created using different types of disturbances, where it is possible to find thermoelectric, acoustic, pneumatic, microfluidic, and piezoelectric droplet generators. The first one applies a short duration electric pulse to a resistive component in contact to the fluid, generating a bubble nucleation [21]. The acoustic type uses a sound source to create the mechanical disturbance [22]. On the other hand, the principle of pneumatic generators is to apply a liquid or gas pressure in the meniscus by the action of a moving component [23]. The microfluidics use two or more immiscible fluids and generate droplets by colliding the fluid that will be broken into small droplets with the immiscible one [24]. Finally, the piezoelectric droplet generators use materials with piezoelectric characteristics that, while vibrating, generates disturbance that implement pressure variations on the fluid chamber or make the outlet section vibrate. This mechanism is the chosen disturbance source for the

present work, and will be explained in more detail.

The piezoelectric droplet generators can be divided into two classes, depending on the type of the droplet generation, the continuous mode and drop-on-demand (DOD) mode. The continuous mode working principle was already explained in the previous sections and the droplet generators presented in the section 1.2.4.2 work with continuous streams. The DOD mode, generates droplets due to pressure by a voltage-pulse driven piezoelectric actuator. The liquid is ejected out of small orifices with pulsed flow rates to form pulsed jets. Similar to the continuous jet generators, in this mode, the droplet generation process is sensitive to signal waveform, nozzle structures and liquid properties [25]. Some droplet generators can operate with the two principles, depending on the work conditions.

The piezoelectric droplet generators can also be divided by the form of deformation that is applied to the system, where it is possible to find four types of deformation modes: sheer mode, squeeze mode, bend mode and push mode. These types of deformation can be used both on the continuous mode and on DOD mode [26].

In the sheer mode droplet generators, the vibration is usually implemented directly on the ejecting fluid. The piezoelectric cell is placed at the outlet of device and changes the nozzle shape while vibrating, as seen in figure 1.5. The shear action deforms the nickel plate against the fluid, thus ejecting the droplets. This type of droplet generators are not easy to machine [27].

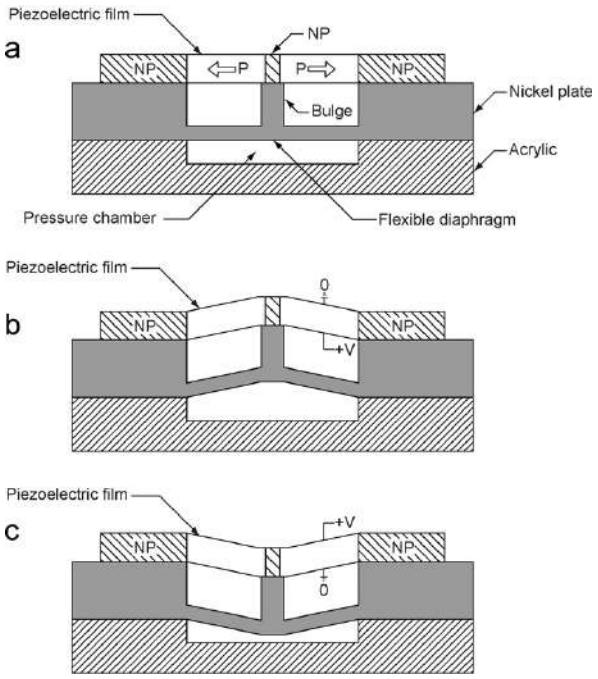

Figure 1.5: A schematic of the polarisation direction of a sheer mode droplet generator [27].

The squeeze mode droplet generators usually use capillary tubes surrounded by a piezoelectric ceramic that squeezes the tube when excited, causing the tube to contract in a longitudinal direction, reducing its diameter, leading to droplet formation. This kind of droplet gen-

erators is usually used to create monodisperse jet breakup, but the concept can be applied to generate drop-on-demand. Some of the droplet generators referred in section 1.2.4.2 were developed with this working principle. Ulmke et al. [28] applied this concept to a drop-on the demand generator that was able to generate small droplet diameters with a range of $10\ \mu m - 100\ \mu m$ without any external pressure. In figure 1.6 it is possible to observe a schematic with the droplet generator structure developed by Wu et al. [23]. This droplet generator was able to produce a monodisperse stream jet and a new regime called "semi-monodisperse droplet formation" was found.

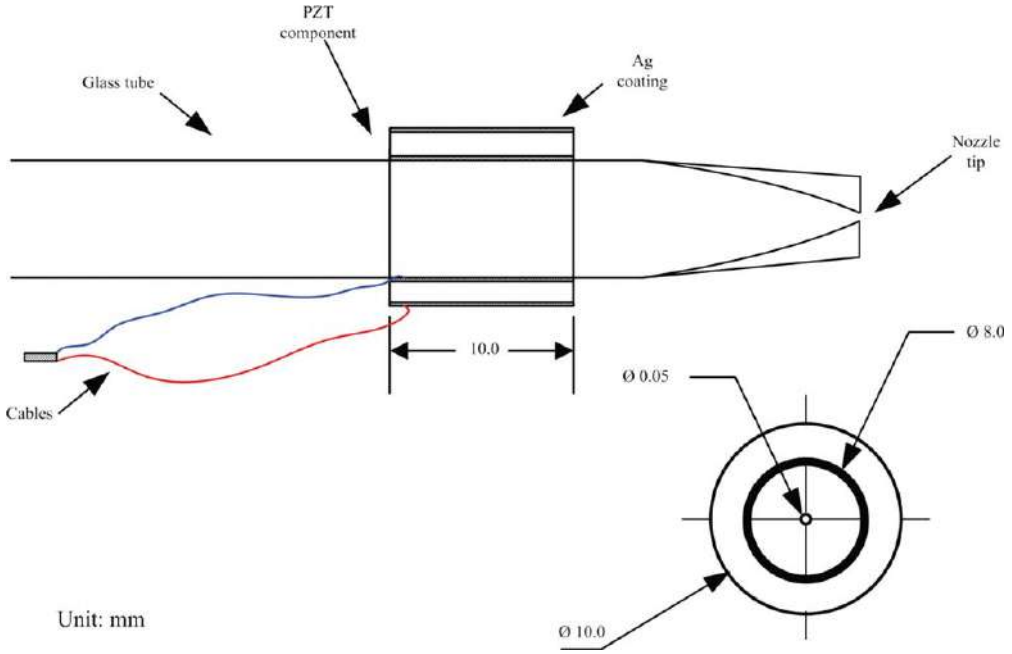

Figure 1.6: Schematic of a squeeze mode droplet generator design [23].

Regarding the bend mode, the piezoceramic plates are bonded to the diaphragm, forming an array of bilaminar electromechanical transducers used to eject the droplets [26]. Laurel et al. [29] developed one bend droplet generator that has two joined silicon structures forming a flow-through channel. One channel wall couples the impulse movement of a piezoceramic element into the flow channel, generating a pressure pulse. Droplets are then ejected from an orifice in the opposite channel wall. Figure 1.7 shows a design for this type of droplet generators.

As for the push mode, in order to achieve droplet generation, the piezoelectric cell, that usually consists of a diaphragm with a piezoceramic disc, is positioned above the liquid and, when a signal is applied to the cell, it vibrates by changing its shape and volume, changing the fluid chamber volume. When the cell expands, the volume of the fluid chamber decreases and creates a positive pressure differential on the fluid. Increasing fluid pressure causes a portion of the fluid to be pushed through the nozzle. When the cell contracts, the volume of the fluid chamber increases again, only to withdraw the fluid. In figure 1.8 it is possible to observe a push mode droplet generator developed by Fan et al. [30], where a thin piezoceramic layer is fixed within the main body and bends where a voltage pulse is applied. The

pressure is generated in the liquid chamber, pushing the liquid out of the glass nozzle.

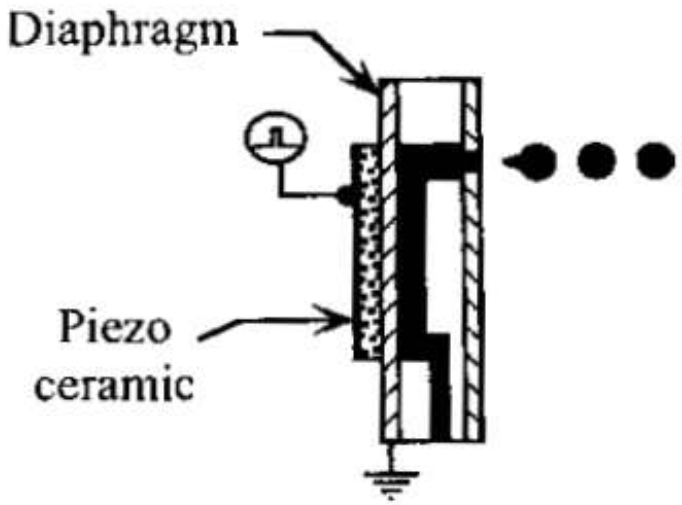

Figure 1.7: A bend mode droplet generator design [26].

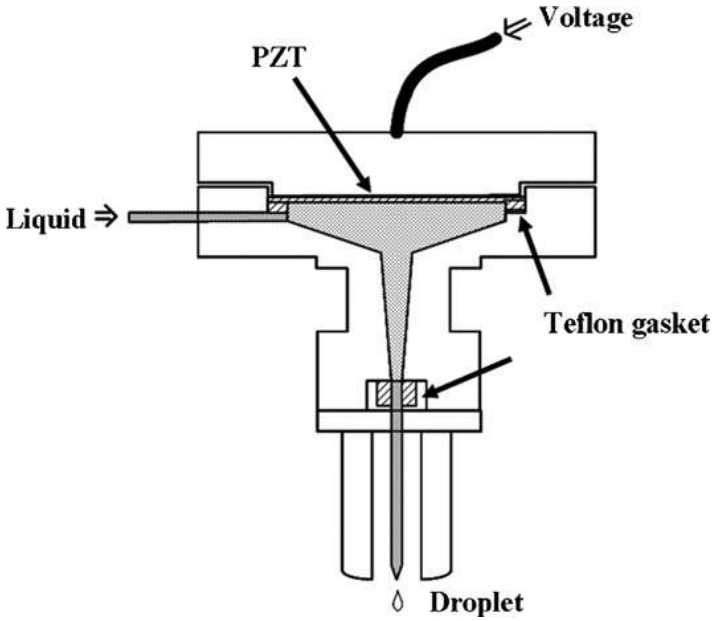

Figure 1.8: Configuration of a push mode generator [30].

1.3 Objectives

As seen in literature review, many stream droplet generators have been developed throughout the years and this is a well known technology. However, many of them have complex working processes and are very expensive. Thus, the main objective of the present work is to optimise a low-cost droplet generator and characterise the monodisperse regime, obtaining a device that can be used for different research applications. The optimisation process has the objective to enable an easy assembly and installation than the previous droplet generator. On the other hand, the characterisation process provides the droplet generator operation limits,

allowing an the device to be easy utilised. In this characterisation process, three different fluids were tested and the last objective of this work is to understand the differences between these fluids.

1.4 Organisation

This dissertation is organised in four chapters. The first chapter concerns the introduction, and explains the motivations of the present work, followed by the literature review, which presents the necessary theoretical information for the work execution and, afterwards, the work objectives.

The second chapter starts with an extended explanation of the droplet generator design, starting with a brief explanation about the previous design and the modifications done, passing by the design and fabrication processes, the all the way to the final assembly of the present design. After, the experimental facility are shown and describe together with the equipment used. Then, the work methodology is presented, and finally, all the methods used to process the experimental data are issued.

In chapter three, the results and discussion are divided in two major parts: visualisation and characterisation. In the first part all the phenomena that were observed in the testing phase is analysed and explained, while the experimental data obtained is organised and analysed in the second part.

Finally, the last chapter presents the work conclusions and possible future works.

Chapter 2

Droplet Generator Design and Experimental Procedures

In this second chapter, the droplet generator design and the different experimental procedures used in the present work will be presented in four different sections: droplet generator, experimental arrangement, methodology and experimental data processing. In the first section, all droplet generator development processes will be explained. Then, the experimental arrangement, the different components used and its specification will be shown. Afterwards, the work methodology will be detailed. Finally, the experimental data processing will be explained and the different methods for the determination of each property will be explained.

2.1 Droplet Generator

In this section, the previous droplet generator design [31] will be briefly explained, as well as the modifications suggested to improve the design. After that, the design developed for the present work, the corresponding fabrication process and the different components used will be explained, ending with the assembly of all parts.

2.1.1 Previous Droplet Generator Design

Moura [31] designed a low cost, push mode piezoelectric stream droplet generator with interchangeable nozzle. In this section, a brief explanation about this design and operation is presented. The device is shown in figure 2.1.

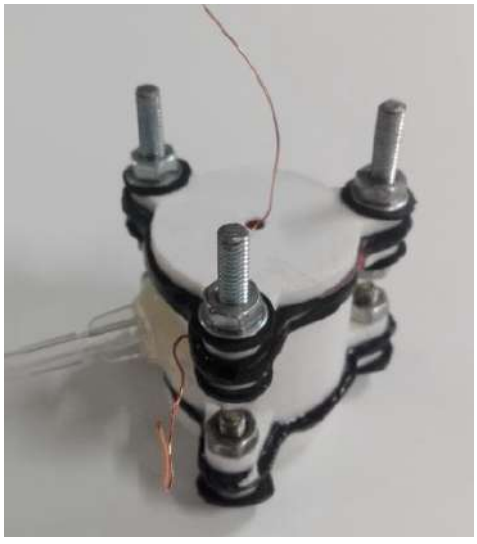

Figure 2.1: Previous droplet generator fully assembled [31].

The droplet generator structure is made of PLA (Polylactic acid) and has four different parts: lid, body, pinhole holder lid (PHL) and pinhole holder base (PHB), as seen in figure 2.2. These structures are connected to each other by bolts (figure 2.1), and between them rubber sealants were used with the objective of containing the fluid. A piezoelectric diaphragm that vibrates through the variation of waveform parameters created by an external signal is placed in the lid structure, creating disturbances directly onto the liquid surface. The fluid is stored in the body component which is connected to a liquid admission cable. The PHB and PHL support the nozzle where the stream droplet jet is generated.

2.1.2 Improvement Modifications

In order to optimize the previous work, it was necessary to assess what characteristics could be modified to improve the device. Most of these characteristics do not affect the droplet generator performance, since it was fully operational already, yet the modifications intend to improve some experimental difficulties that the previous design had. Therefore, these characteristics are listed below:

- The use of a three-holed extension configuration (figure 2.2) caused difficulties in the image acquisition process whenever the bolts were aligned with the camera plane, preventing the light to reach the jet. Therefore, a specific position and arrangement for the droplet generator installation was required in order to acquire well illuminated images;

- Pinhole holder lid (figure 2.2a) and body (figure 2.2b) are two different parts. Given that the droplet generator needs to contain liquid inside, it is desirable to have the least parts possible;

- The sealants are made manually from rubber sheets. The size precision can be increase by using a different material and method of production;

- Using the lid component (figure 2.2a) as piezoelectric support. It is crucial to place the piezoelectric diaphragm in a centered position so the disruptive waves can be applied evenly into the liquid surface. To achieve that, the piezoelectric diaphragm must be aligned with the body part, which can be difficult to attain when the piezoelectric diaphragm have a support to be placed as in the referred lid part;

- The lid component (figure 2.2a) is made of PLA. This component suffers a lot of tension due to the tightness of the bolts, possibly leading to the break of the component.

Different changes were made with the objective of improving the previous design and overcome the manufacture and experimental difficulties listed previously. These changes are mentioned below:

- The use of three-holed extension configuration was modified to a four-holed extension configuration. This change allowed to overcome image acquisition difficulties because

the bolts are all aligned with each other and not with the camera plane;

- The pinhole holder lid and the body were merged, resulting in a single part, simplifying the device structure and removing the need to use more sealants between these parts;

- The sealants are printed in a 3D printer using Filaflexible 40, a flexible material that uses a combination of plastic and rubber. This allowed great precision in the sealants manufacturing;

- The lid part was separated into two different components: the superior lid part and the inferior lid part and the piezoelectric diaphragm is now placed in the upper section of the body. All the parts will be detailed in the next subsection;

- The piezoelectric diaphragm was changed to a diaphragm with a larger diameter. This change was not related with experimental difficulties but rather a choice of available material.

In this section are only presented the changes made to the previous design with a brief explanation, however, in the next section, all new parts dimensions and functions will be detailed.

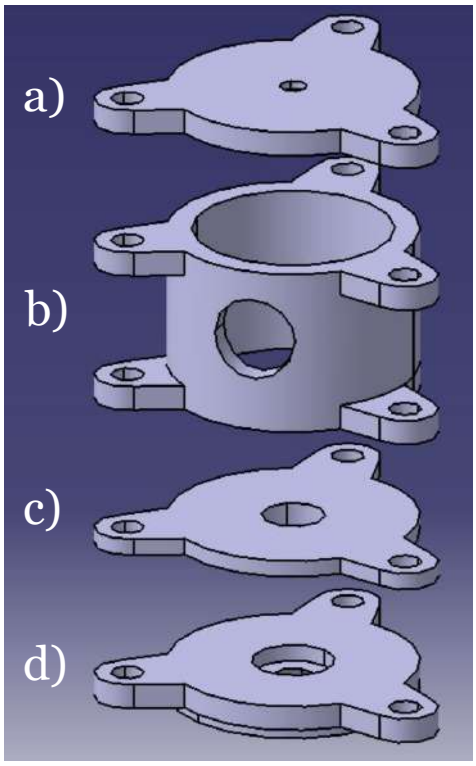

Figure 2.2: Parts of a previous design that use a three-holed extension configuration. a) Lid part; b) Body part; c) Pinhole holder lid; d) Pinhole holder base [31].

2.1.3 Droplet Generator Design

The device was designed using the CAD software CATIA v5 where all the parts were drawn separately and then assembled together to ensure all dimensions were correct. The device has 4 different parts: superior lid part (figure 2.3), inferior lid part (figure 2.4), body (figure 2.5), and pinhole holder (figure 2.6). The superior lid part is the top part of the dispenser that has the objective of pushing the inferior lid part against the body, sealing the device. The inferior lid part has the function of sealing the fluid chamber located in the body part. Thus, the body part is the central part of the droplet generator by allocating the fluid chamber, establishing the connection between the liquid chamber and the pinhole holder, and supporting the piezoelectric diaphragm. Finally, as the name suggests, the pinhole holder part main function is to hold the stainless steel pinhole, that work as a nozzle for the droplet generator. Other smaller parts were designed as connection parts and will be explained in the next section. All the technical drawings are presented in the figures 2.3 to 2.6 for each part.

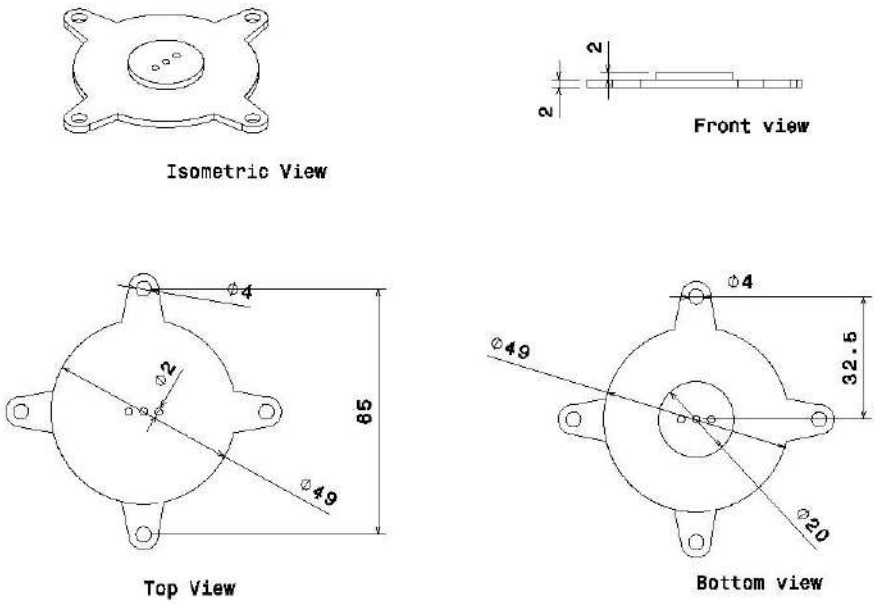

Figure 2.3: Superior lid part technical draw with isometric, front, top and bottom views (units in mm).

As stated earlier, the actual design is inspired in a previous work, therefore, both devices share many similarities such as the structure format. The body main structure dimensions and form were chosen in order to match the piezoelectric diaphragm measurements and geometry, shown in subsection 2.2.4. The rest of the parts were built from this requirement utilizing an iterative process, where different dimensions were tested, to reach the final dimensions presented in the figures 2.3, 2.4, 2.5, and 2.6 . The pinhole holder hole dimensions were set in order to match the pinhole dimensions, presented in subsection 2.1.6.

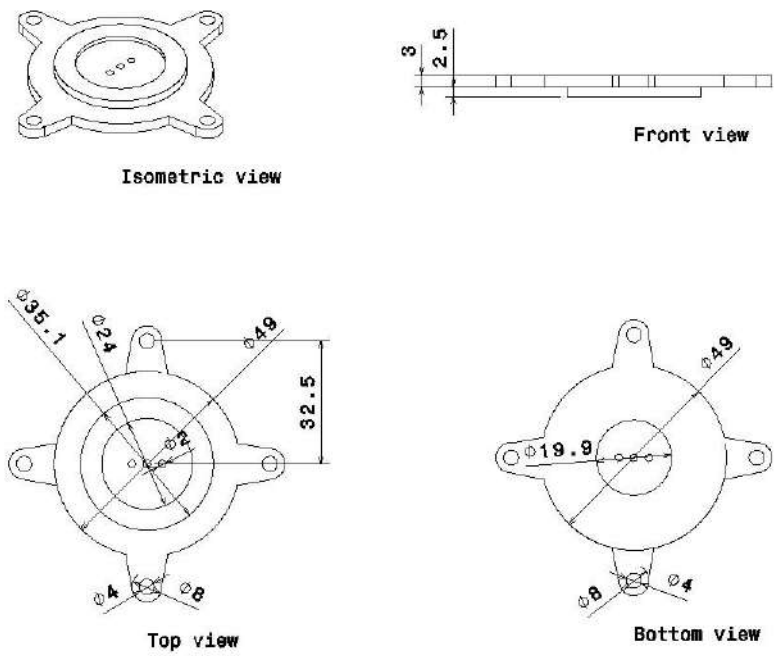

Figure 2.4: Inferior lid part technical draw with isometric, front, top and bottom views (units in mm).

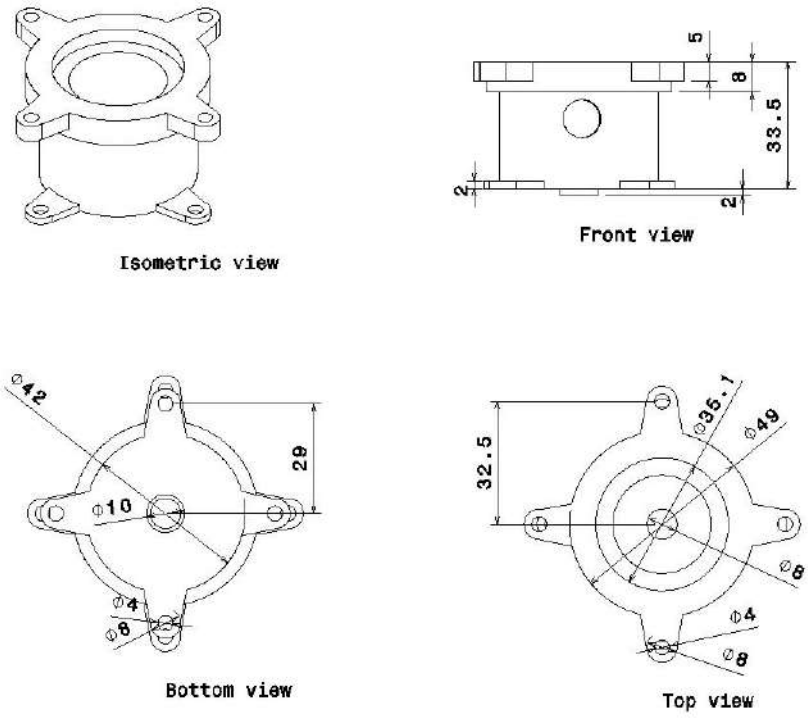

Figure 2.5: Body part technical draw with isometric, front, top and bottom views (units in mm).

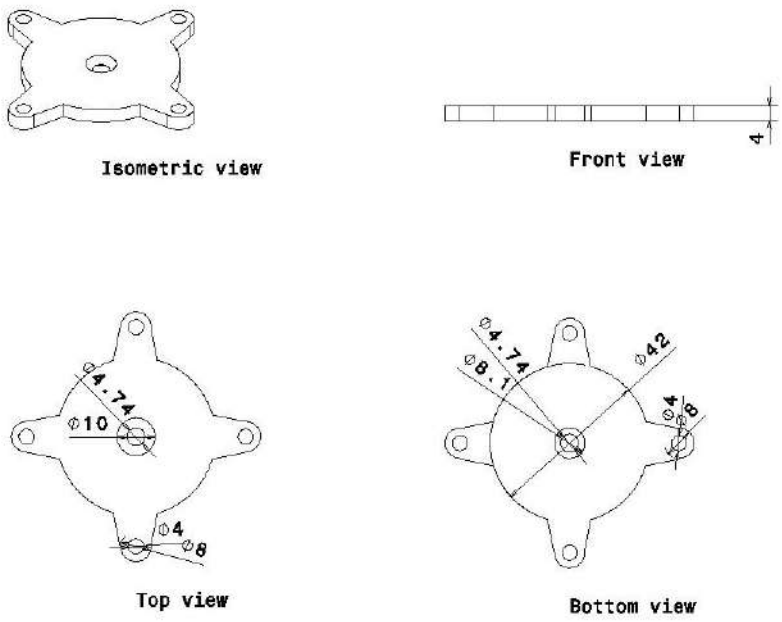

Figure 2.6: Pinhole holder part technical draw with isometric, front, top and bottom views (units in mm).

2.1.4 Fabrication

The parts described in the previous section were all printed using the 3D printer Prusa i3 MK3. Two different 3D printable materials were used in the fabrication process: PLA and FilaFlexible40. PLA (Polylactic acid) is renewable and biodegradable material with good thermomechanical properties [32] and FilaFlexible 40 is a flexible and rubber-like material [33]. Both material properties are presented in the annex A.1.

Three different parts were printed using PLA: body (figure 2.7a), superior lid part (figure 2.7b), and pinhole holder (figure 2.7c). These parts were built with PLA because they have to be rigid in order to fulfill their function. As stated previously, the superior lid part function is to push the inferior lid part, closing the device. Therefore, this part needs to have good mechanical properties to meet its purpose, without changing its geometry. On the other hand, the body component has to contain the liquid chamber that suffers high internal pressure, thus a rigid material with good mechanical properties is needed. Lastly, the pinhole holder must maintain its geometry so the final assemble could be performed successfully.

For the parts that need to be flexible, Filaflex 40 was the chosen material. The inferior lid part (figure 2.8a) was printed with this material since this part acts not only as a structural part, but also as a sealant, thus, it needs to be flexible in order to seal the device. The other parts printed with this material are presented in figure 2.8b. These parts are placed between the structural parts presented in the section 2.1.3 acting as sealants. The part shown in figure

(a) (b) (c)

Figure 2.7: Parts fabricated with PLA. a) Body part; b) Superior lid part; c) Pinhole holder part.

2.8b I was the sealant used between the body part and the pinhole holder part and has a 1 mm thickness. The part shown in figure 2.8b II is used between the body part and the inferior lid part and has a thickness of 0.85 mm. Lastly, the part in figure 2.8b III were used on the pinhole holder to accommodate the pinhole and both have a thickness of 0.6 mm.

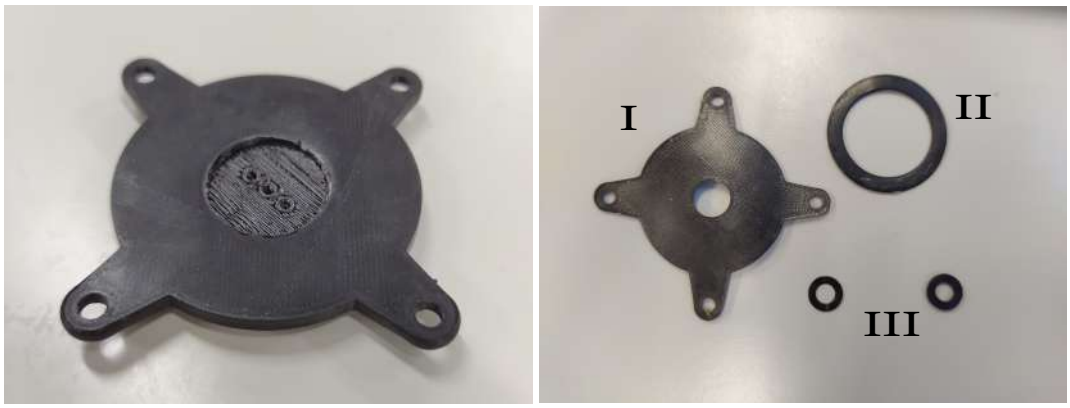

(a) (b)

Figure 2.8: Parts fabricated with FilaFlexible40. a) Droplet generator inferior lid part; b) O-rings.

2.1.5 Disturbance Source

A piezoelectric diaphragm, which generates disruptive waves through the variation of waveform parameters, was placed above the liquid chamber, generating disturbances directly onto the liquid surface in a parallel direction, making this device a push mode generator. For the present work, a piezoelectric diaphragm, with a part number SMPD3SD35T25F18 (figure 2.9), acquired from STEMINC, was used as the disturbance source.

This component consists of a piezoelectric ceramic plate which has electrodes on both sides and a metal plate. The metal plate (outer diameter), represented as D in figure 2.9a has a diameter of $35\ mm$ and a thickness of $0.10\ mm$ (represented as as t), whereas the ceramic plate (inner diameter) represented as d, has a diameter of $25 mm$ and its maximum thickness, represented as T, is $0.22\ mm$. Two copper wires were weld to both ceramic and metal plates, allowing the external signal to excite the piezoelectric diaphragm.

(a)

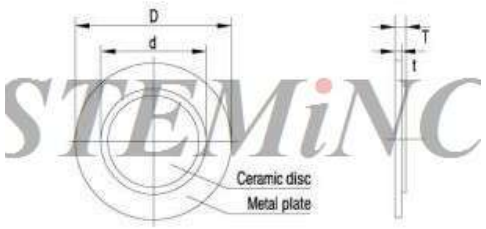

(b)

Figure 2.9: Disturbance Source a)Piezoelectric diaphragm; b) Piezoelectric dimensions; [34].

2.1.6 Nozzle

One of the most important characteristics of the droplet generator is the interchangeable nozzle. The interchangeable nozzle used was a round stainless-steel high precision optical pinhole (figure 2.10) with three different inner diameter sizes: $100\ \mu m$, $150\ \mu m$, and $200\ \mu m$. All three pinholes have the same dimensions with an outer diameter of $9.5mm$ and a thickness of $0.03\ mm$. The pinhole holder component is separated from the liquid chamber and the nozzle can be easily changed, enabling the cleaning/unclogging of the nozzle or allows the exchange between nozzle sizes.

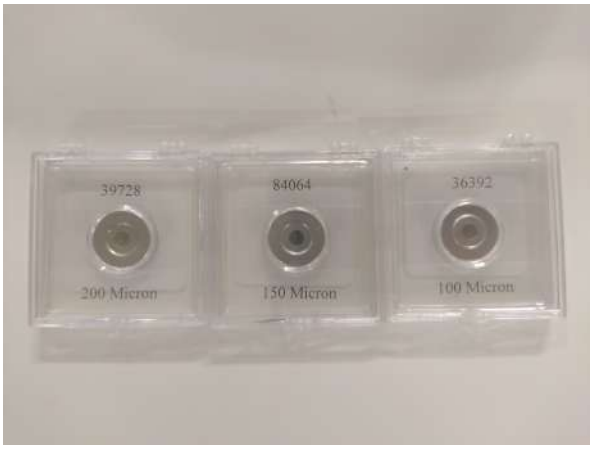

Figure 2.10: Stainless-steel high precision optical pinholes with an inner diameter of $200\ \mu m$, $150\ \mu m$, and $100\ \mu m$.

2.1.7 Final Assembly

In this section, the device final assemble is detailed. The assemble is divided in two different groups: piezoelectric ensemble and nozzle ensemble. Initially, a medical tube was inserted and glued to the admission hole located in the body part, as seen in the figure 2.7a. After that, an O-ring (figure 2.8b) was placed in the body upper hole to accommodate the piezoelectric diaphragm which is wrapped in a water resistant material before its placement in the body part. After placing the piezoelectric, the superior and inferior lid parts are mounted together and placed above the body part, passing the copper cables inside the holes, as seen in figure

2.11. Then, the structures (both lid parts) are assembled to the body part using bolts and nuts, as seen in figure 2.11, finishing the assemble of the piezoelectric ensemble. Thereafter, the O-ring (figure 2.8b) is aligned with the pinhole holder part and the stainless steel pinhole is placed in the pinhole holder hole between two small O-rings (figure 2.8b). Finally, both parts are assembled with nuts and bolts. The second ensemble (nozzle) must be disassembled after every use while the first ensemble must be kept assembled with the exception of some maintenance processes.

Figure 2.11: Droplet generator fully assembled.

2.2 Experimental Arrangement

An experimental setup (figure 2.12) was designed and built to obtain the validation of the device. The present section shows this setup and issues the different components used for these experiments. This setup can be divided in four parts: image acquisition system, dispensing system, lighting setup and disturbance source. All parts are detailed in the following subsections. The droplet generator has a support made of PLA that is connected to an iron beams structure as shown in figure 2.13. This structure also supports the syringe pump while the signal generator, temperature sensor and computer are supported by a table. On the other hand, the halogen lighting unit is supported by a tripod behind a diffuse glass placed in the iron beam structure, lighting up the testing site. The camera is facing the droplet generator and it is triggered manually while all images are saved in the computer that is connected to the camera.

Figure 2.12: Experimental Arrangement: 1) Computer; 2) Signal generator; 3) Temperature sensor; 4) Halogen lighting unit; 5) High-speed digital camera; 6) Syringe pump; 7) Droplet generator; 8) Picoscope tip; 9) Liquid reservoir; 10) Diffuse glass.

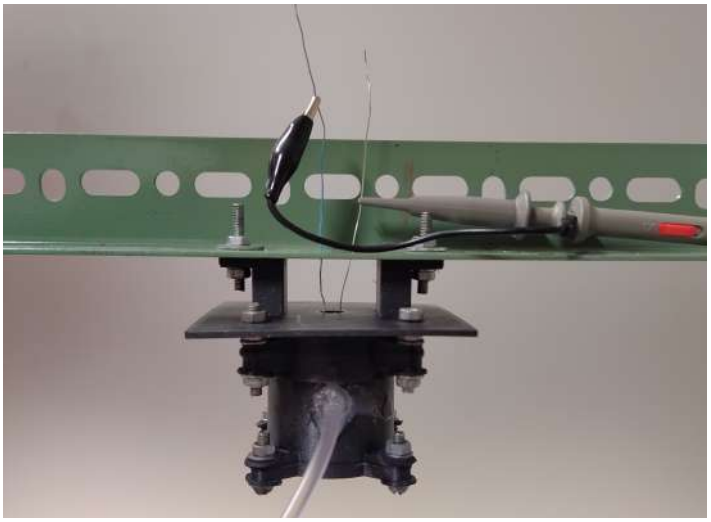

Figure 2.13: Droplet generator attachment support.

2.2.1 Image Acquisition System

Image acquisition is one of the most important parts of these experiments. To assure results with high precision and quality, an assembly of a high-speed digital camera and a macro lens were used (figure 2.14). The camera Photron FASTCAM mini UX 50 has 1.3 Megapixel of resolution when working at 2000 frames per second (fps) and reduced resolution all the way to frame rates of 160000 fps. The Macro Lens Tokina AT-X AF PRO D was connected to the camera and has the following specifications: a minimal focus distance of 0.3 m, a focal length of 100 mm, a filter size of 55 mm, and a 1:1 macro ratio.

Figure 2.14: Photron FASTCAM mini UX 50 and Macro Lens Tokina AT-X AF PRO D.

The values of time exposure (shutter) and frame rate (fps) were set at 1/80000 s and 25000 fps, lowering significantly the resolution to 1280x96 for most part of the experiments. However, when the 100 µm pinhole was used with high flow rate, the resolution was even lower than before, since the shutter and frame rate used were 1/160000 s and 40000 fps, leading to a resolution of 1280x56. This was necessary because a large number of images is needed for the velocities calculation and the shutter plays a significant role when capturing images of moving objects. With this in mind, a compromise between minimum exposure to the light and resolution was needed.

2.2.2 Dispensing System

The dispensing system is the key to create the droplet stream and to select what types of conditions one might use. Three different components are part of this system: droplet generator, described in the chapter 2.1, syringe pump (figure 2.15) and medical tubes.

The syringe pump NE-1000 was used to control the intake flow rate. This pump presents a maximum and minimum pumping rate as low as $0.73\ \mu l/hr$ with a $1\ ml$ syringe or as high as $35.33\ ml/min$ with a $60\ ml$ syringe. For the present experiment, a $50\ ml$ syringe was used, as it is shown in figure 2.15, employing different flow rates according to the different needs.

Figure 2.15: Syringe Pump NE-1000.

This syringe is connected to the droplet generator through medical tubes, transporting fluid to the device.

Three different fluids were used in the experimental tests: distilled water, jet fuel, and a mixture of biofuel and jet fuel. The jet fuel (JF) chosen was Jet A-1 and the biofuel was HVO (Hydroprocessed Vegetable Oil). The mixture has 50% volume of jet fuel and 50% volume of biofuel. This was the chosen mixture due to the current legislation only allowing the use of a jet fuel and biofuel mixtures in the aeronautical sector with 50 % of jet fuel [35]. The fluids properties were measured by Ribeiro [36] and are presented in table 2.1. All these properties were measured in a controlled environment, under the following conditions: temperature at 22 ^{o}C ± 1^{o}C and humidity at 50%.

Table 2.1: Water, jet fuel and a mixture of jet fuel and biofuel respective properties (surface Tension, density and viscosity) [36].

Fluid	**Fluids properties**		
	$\sigma\ [mN/m]$	$\rho\ [kg/m^3]$	$\mu\ [Pa.s]$
H_2O	71.97	1000.0	0.001003
100% JF	25.37	798.3	0.001120
50% JF / 50% HVO	24.64	792.4	0.001790

2.2.3 Lighting Setup

Illumination is one important part of testing because the filming requirements in these experiments are really high due to the droplet size and velocity, being desirable to get well illuminated images so the different regimes could be identified and the analysis process could be achieved with less errors. For this purpose, an halogen lighting unit (figure 2.16) was used behind a diffuse glass shown in figure 2.12 with the objective of diffusing and scattering the light. The kaiser videolight 6 uses a 1000 W halogen lamp and has an extremely quiet cooling blower for unlimited operation in every position and a thermostat for automatic shut-off in case of overheating.

Figure 2.16: Kaiser videolight 6.

2.2.4 Disturbance Source

The piezoelectric cell needs to be excited in order to create a disturbance onto the liquid surface. This can be achieve using the PeakTech 4115 signal generator, connected to a picoscope tip, as can be seen in the figure 2.17. The signal generator allows the user to control different wave properties: wave shape, wave frequency, and wave amplitude. The piscoscope tip is then connected to the piezoelectric cell copper cable, enabling the piezoelectric diaphragm to excite.

Figure 2.17: Signal Generator PeakTech 4115.

2.3 Experimental Methodology

In the experimental testing, image acquisition was used in order to accomplish two different experimental parts, the first being the visualisation of the different phenomena, for example monodispersity or secondary droplets formation, and the second being the measurement of the jet properties for the monodisperse cases such as droplet diameter, droplet velocity, distance between droplets, continuous jet length and finally, the calculation of the dimensionless numbers that govern the different phenomena. In the first phase of testing, two different pinholes were tested ($150\ \mu m$ and $200\ \mu m$) using distilled water and the following steps were strictly executed:

1. Choose one pinhole size and assemble the droplet generator;

2. Illuminate the testing site, align the diffuse glass behind the droplet generator and turn off all lights in the room, making the illumination created for these experiments to be the only light source in the room, avoiding some interference such as shadows;

3. Place the high-speed camera in front of the droplet generator and adjust the distance to the testing site;

4. Acquire a background image and an image with a reference to calculate the pixel size;

5. Connect the droplet generator to the syringe pump and start the pumping at a low pump rate (1.5 mL/min);

6. Let the device running for some time to fill the fluid chamber and to stabilise the jet;

7. If the droplet generator is dripping, add 1 mL/min to the flow rate until stream jet is found - the maximum flow rate is 6.5 mL/min in order to preserve the structural reliability since the pressure in the liquid chamber increases with the intake flow rate;

8. Acquire images using the high-speed camera. Take five tests for each flow rate tested;

9. Connect the piezoelectric ceramic to the signal generator using the maximum amplitude and a square wave in order to maximise the instability, and set the syringe pump to the first flow rate value where stream jet is observed.;

10. Change the wave frequency and acquire five different tests for each relevant phenomenon;

11. Repeat this last step for the different flow rates tested initially;

12. Disassemble the droplet generator and clean the nozzle.

In the second phase of testing, two more fluids were used: jet fuel and a mixture with jet-fuel and HVO. The steps stated before were followed in the same manner as in the first phase. In the final phase, a 100 μm pinhole was tested using the same fluids used before, but the image capture characteristics changed: the camera was moved closer to the testing site and the lighting unit was placed in a different position in order to get more light allowing a higher frame rate and a lower shutter to be used. This was necessary because the stream velocity in these conditions is significantly higher than in the previous conditions, in which the latter resulted in images poorly focused and more than one droplet would be formed for each frame.

2.4 Experimental Data Processing

As mentioned earlier, the images acquired must be analysed so the different parameters (diameter, velocity, etc) can be determined and, therefore, fully characterise the monodisperse regimes for the different conditions.

To achieve that, an algorithm was used to treat the images using binarisation and the different calculation methods for each property will be explained in this section.

2.4.1 Pixel Sizing

This is an important step in this analysis because pixel size is the measurement unit used to obtain the properties values. To establish the pixel size, a reference was used with a known value. This reference is a stainless steel dispensing needle with a 510 µm outer diameter and can be observed in figure 2.18.

Figure 2.18: Stainless steel dispensing needle with an outer diameter of $D_{out} = 510\ \mu m$.

Using the software MATLAB, a code was written to calculate the number of pixels of the needle outer diameter and then the real pixel size is obtained using equation 2.1.

$$\text{Pixel Size} = \frac{\text{Outer Diameter (mm)}}{\text{Number of Pixels}} \quad (2.1)$$

First, the code reads the original image (figure 2.19a) and transforms this image into a matrix of ones and zeros (binarisation) each one corresponding to one pixel. The ones in the matrix correspond to the white pixels and the zeros correspond to the black area, resulting in a well defined figure as shown in figure 2.19b. Then, a section of the figure is chosen in order to obtain the value of pixels that correspond to the needle outer diameter. As stated before, the

outer diameter value in microns are divided by this value, obtaining the pixel size.

This pixel size is not the same for every image because the distance between the high-speed camera and testing site may change according to the test conditions. For example, the camera needs to be closer to the testing site with a smaller nozzle. Due to this, the pixel size is calculated for each condition to ensure precision in the results and both the camera and the device were kept static for the 5 different tests for each condition, resulting in the same pixel size for all five tests. In these experiments, a range of values were utilised and each pixel can correspond from $11\ \mu m$ to $27 \mu m$.

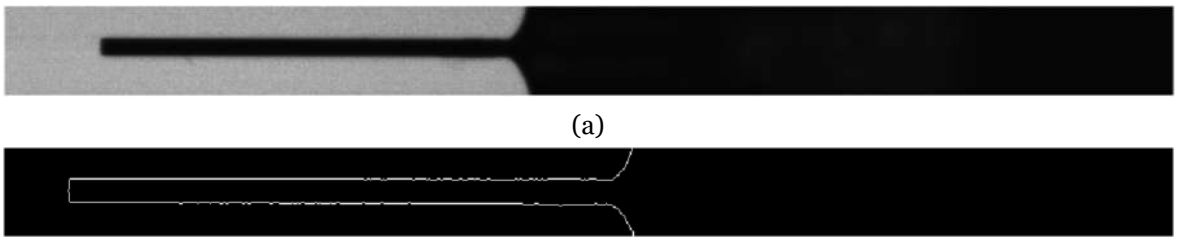

(a)

(b)

Figure 2.19: Pixel sizing process. a) Original reference image; b) Resulting binary gradient.

2.4.2 Droplet Diameter Calculation

The droplet diameter calculation is an essential part of these experiments. In order to achieve that, a similar algorithm to the one explained in the previous subsection was developed, with the addition of the necessary tools to calculate the droplets diameter.

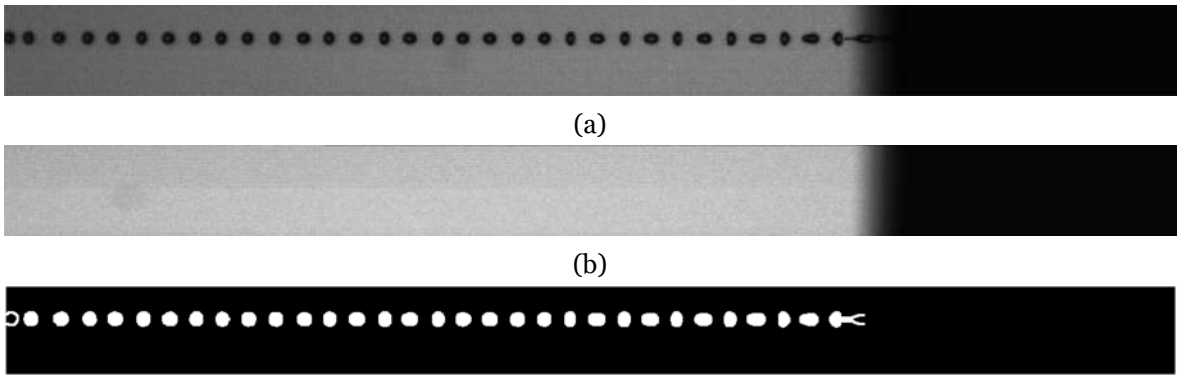

(a)

(b)

(c)

Figure 2.20: Image processing. a) Matlab image reading; b) Background image reading; c) Binaray gradiant mask.

The first step is to choose the images that will be analysed. Two images for each experimental test were selected, excluding images with defects, and ten different images were analysed simultaneously. The original image (figure 2.20a) is read and then subtracted to a background image (figure 2.20b) in order to isolate the droplets. After that, the subtracted image (figure 2.20c) is transformed into a matrix with ones and zeros (binarisation), similar to the process stated in the section 2.4.1, generating a black and white image (figure 2.20c). The major and minor axes were calculated by counting the pixels for each droplet in the figure and the mean

value of the two axes corresponds to the droplet diameter. After that, all droplets diameter value are averaged, getting the mean droplet value of the jet. All ten analysed figures are submitted to this process and subsequently an overall diameter mean value is obtained for each figure. The final diameter value is the arithmetic mean of the diameter value of each figure, and is then multiplied by the pixel size, obtaining the final diameter.

2.4.3 Distance Between Droplets Calculation

As stated in chapter 1.2.4, a jet is considered monodisperse when the droplets generated have the same diameter and the same distance between them. Given that, the determination of the distance between droplets is essential to fully characterise the droplet generator. The MATLAB algorithm explained in section 2.4.2 was utilised in this parameter calculation with the addition of a new calculation method. The first part of the code is the same as the one stated in section 2.4.2 where the image is processed (binarisation process), generating an image as figure 2.20c, and the droplet diameter is calculated. The second part determines the centroid of each droplet in the image, saving every droplet position. After that, the distance between droplets (s in figure 2.21) were calculated subtracting the distance between centroids (L in figure 2.21) for the prior droplet diameter (D in figure 2.21). All distances are determined in the same manner and a mean value is calculated for each figure and an average value is obtained for all tests. This value is then multiplied by the pixel size in order to obtain the real distance between droplets. The image selection for this process follow the same method in the droplet diameter calculation.

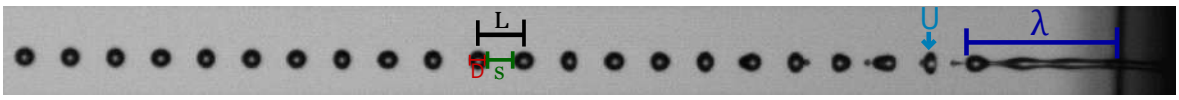

Figure 2.21: Image analysis scheme.

2.4.4 Velocity Calculation

The jet initial velocity is a necessary part of this analysis given that different conditions such as pinhole size and inlet flow rate modify significantly the velocity which is an important term in the governing parameters (Reynolds number, Weber number and Ohnesorge number) calculation.

A part of the MATLAB algorithm explained in the previous section was used in the velocity calculation process in order to obtain the centroid coordinates for each droplet in the different analysed images.

In addition, ten sequential images were chosen and in the first image, the first droplet was isolated (U in figure 2.21) and its centroid coordinate was saved. Then, in the next images, the centroid of the same droplet was saved as well, and with the position of the centroid in every image, the velocity in pixel/s for each position can be determined using the equation 2.2. Then, a mean velocity value is obtained for each test.

$$\text{Jet Velocity} = \frac{\text{Distance Between Centroids}}{\frac{1}{\text{Frame Rate}} \times \text{Number of Frames}} \quad (2.2)$$

In order to get the maximum precision, five different sets of ten images were measured for each monodisperse condition obtaining a final velocity value, which is multiplied by the pixel size, obtaining the velocity in meters per second. Then, the dimensionless numbers are calculated using this value.

2.4.5 Continuous Jet Length Calculation

The last parameter needed to characterise the droplet generator is the jet continuous length. As seen in chapter 1, this parameter is the result of a natural disturbance and the external disruptive waves, changing its value for different conditions. This is important to analyse since it can provide a measure of growth rate of the disturbance.

Similar to the rest of the analysis, a MATLAB code was developed in order to determinate the characteristic disturbance length. The first part was the same as the first part of the algorithm explained in the section 2.4.3. The second part consists in counting the number of pixels that corresponds to the disturbance length (figure 2.21).

The images analysed in this chapter need to correspond to the exact moment before the droplet detachment, in order to obtain the real disturbance characteristic length value. To obtain a good precision, ten different images were analysed for each case of study and a mean value is obtained and is then multiplied by the pixel size, giving the final disturbance characteristic length.

Chapter 3

Results and Discussion

In this chapter, the results obtained from experimental tests will be presented. These experiments were obtained using the device shown in section 2.1 and all data was analysed with the methods described in section 2.4. The analysis is divided into three different sections: phenomena visualisation, monodisperse regime characterisation, and continuous jet part analysis. In the first section, images of the different phenomena for different conditions (fluids, pinhole size, flow rate, frequency range) will be presented and the monodisperse regimes will be detailed. In the second section, the monodisperse regimes will be fully characterised, where the droplet diameter, distance between droplets, velocity and governing parameters are presented and then compared with theoretical values. Lastly, a brief analysis to the behavior of the jet continuous part in the free liquid jet phenomenon will be presented.

3.1 Visualisation

This section is crucial in providing a validation for the different phenomena that can be obtained with a droplet generator, as the one used to execute this work. Different phenomena are presented in this chapter, however, the monodisperse stream jet phenomena will be detailed more deeply, given that studying this phenomena is the present work main objective.

As stated previously, three different fluids and three pinhole sizes were used in the testing phase. The fluids were distilled water, jet fuel (JF) and a 50 % jet fuel and 50% biofuel mixture. All the results will be presented for each fluid and the differences between them will be discussed. The pinhole used have a diameter of $200\ \mu m$, $150\ \mu m$, and $100\ \mu m$. Similarly to the different fluids, the differences in jet formation while using different pinhole sizes, will also be analysed.

3.1.1 Free Jet Formation

In the initial tests, the piezoelectric diaphragm was not excited, allowing the visualisation of the free liquid jet caused only by the device natural disturbances, which are generated by the pressure inside the fluid chamber. This process allows to understand the influence of the different properties, such as fluids properties, pinhole sizes and inlet flow rate, on the jet formation process.

Figure 3.1 shows three liquid jets that were acquired using the same fluid (jet fuel and biofuel mixture) and the same pinhole size ($200\ \mu m$), changing the inlet flow rate for each case, which

starts at $3.5ml/min$ for figure 3.1a, up to $5.5ml/min$ for figure 3.1c. It can be observed that an increase in the inlet flow rate, increases the continuous length size and appears to decrease the jet droplet diameter. In his early studies, Savart [3] showed that, if the jet diameter is kept constant, the length of the continuous part of the jet is proportional to the jet velocity. Thus, the analysed jets have the expected behaviour, given that increasing the inlet flow rate increases the jet velocity and, therefore, increasing the jet continuous length.

Figure 3.2 shows the variation of the pinhole size, starting with the larger one in figure 3.2a up to the smaller one (figure 3.2c), using the same fluid (fuel and biofuel mixture) and a constant flow rate ($3.5\ ml/min$). It can be observed that the jet continuous length grows as the pinhole size decreases, whereas the droplet diameter is smaller when a smaller pinhole size is used. The continuous length can be explained by Savart [3] experiments, which showed that the jet continuous length is directly proportional to its diameter while keeping a constant jet velocity. However, in the figure 3.2, all three images were obtained using the same inlet flow rate and different pinhole sizes, resulting in a different velocity for each one. Hence, it is possible to conclude that, for the present work, the velocity has more effect in the continuous length size than the nozzle diameter. On the other hand, the droplet size difference between pinhole sizes was expected because, the nozzle size in this type of breakup is the most important parameter for jet formation. Rayleigh [5] showed that the droplet diameter can be almost twice the size of the nozzle diameter.

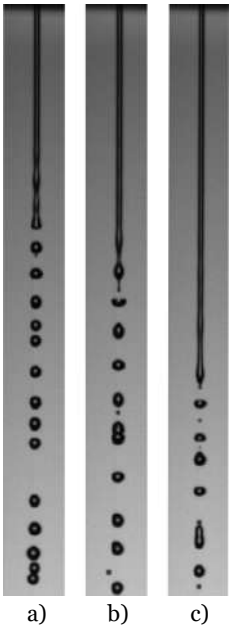

Figure 3.1: Free liquid jet formation using a jet fuel and biofuel mixture and a pinhole size of $200\ \mu m$ with different flow rates. a) $3.5\ ml/min$ b) $4.5\ ml/min$ c) $5.5\ ml/min$.

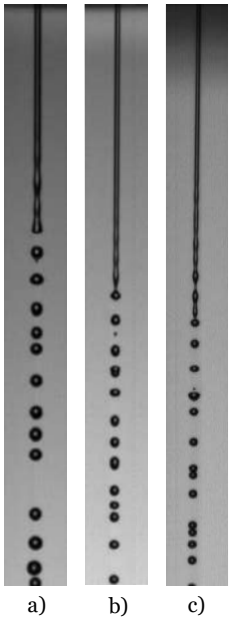

Figure 3.2: Free liquid jet formation using jet fuel and biofuel mixture and a flow rate of $3.5\ ml/min$ with different pinhole sizes. a) $200\ \mu m$; b) $150\ \mu m$; c) $100\ \mu m$.

A comparison between fluids is not presented in this section since it was not possible to compare three images where the camera had the same distance to the testing site, given that the camera was adjusted for each fluid. However, a comparison for the different liquids will be presented in the next section and the influence of the fluid properties in the jet formation

will be discussed in subsection 3.1.3.

Figures 3.1 and 3.2 were obtained using 25000 frames per second and 1/80000 seconds of exposure time. The camera was set at the same distance for every image but its positioning could change depending on different conditions. The lighting position was set in order to obtained the best illumination for each case. The camera positioning and the illumination do not change the high-speed camera working conditions, allowing a comparison between the presented images.

3.1.2 Secondary Droplets

In this regime, for each wavelength of an unstable disturbance, one main droplet and one or more, usually smaller droplets, referred to as satellite droplets, are generated. This can be observed in the figure 3.3.

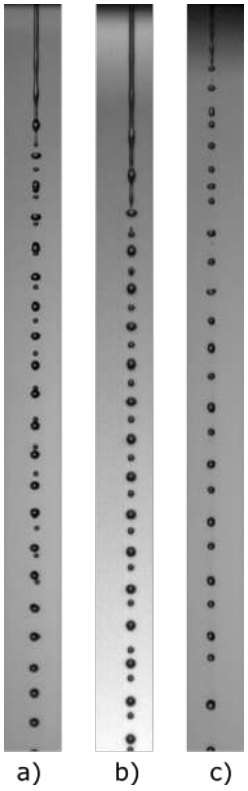

Figure 3.3: Satellite droplets visualisation for different fluids. a) Jet fuel; b) Jet fuel and biofuel mixture; c) Water.

Figure 3.3 shows three different jets, one for each fluid, which were obtained with different conditions in order show that this phenomenon appears for different working conditions. For the figure 3.3a, the following conditions were used: a pinhole size of $150\ \mu m$, an inlet flow rate of $3.5\ ml/min$, and an piezoelectric diaphragm frequency of $3\ kHz$. On the other hand, for the figure 3.3b, the following conditions were used: a pinhole size of $100\ \mu m$, an inlet flow rate of $3.5\ ml/min$ and a frequency of $6\ kHz$. For figure 3.3c, a pinhole of $100\ \mu m$ with a inlet flow rate of $2.5\ ml/min$ and a frequency of $3\ kHz$ were the working conditions used.

It can be observed in the three images that, for each regular droplet formation, a satellite droplet was generated. This pattern is a particular case for the secondary droplets formation and it was only observed when the auxiliary disturbance source (piezoelectric diaphragm) was enabled. The pattern was mostly visualised before the occurrence of the monodisperse cases. Nonetheless, secondary droplets were observed for the free liquid jet case, as seen in figures 3.1 and 3.2 with no notable pattern.

3.1.3 Monodisperse Regime

For this study, this regime is the most important among all regimes obtained with the droplet generator and has two important characteristics: the droplets have the same diameter and they are equally distanced from each other, as seen in figures 3.4 and 3.5. In order to generate a stream jet with these characteristics, all the natural disturbances were not sufficient to disturb the jet in a controlled Rayleigh-type jet break-up manner. Therefore, an additional disturbance source was needed so that the monodisperse regime could be reached. This disturbance source is obtained using the piezoelectric diaphragm at different wave frequencies.

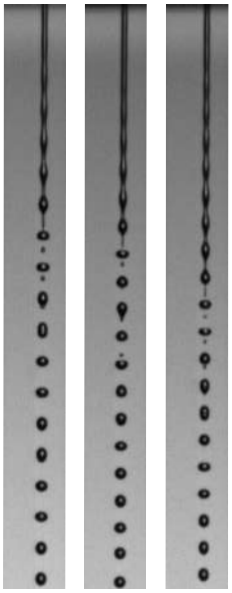

Figure 3.4: Controlled jet formation using jet fuel and biofuel mixture and a pinhole size of $150\ \mu m$ with different flow rates: a) $3.5\ ml/min$; b) $4.5\ ml/min$; c) $5.5\ ml/min$.

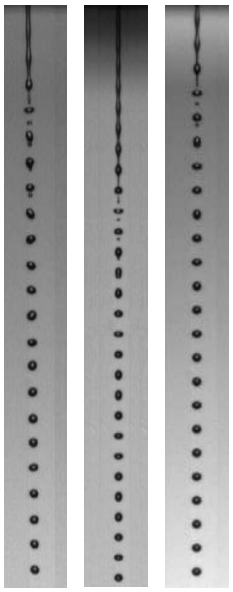

Figure 3.5: Controlled jet formation using a flow rate of $3.5\ ml/min$ and a pinhole size of $100\ \mu m$ with different fluids. a) Water; b) Jet Fuel; c) Jet fuel and biofuel mixture.

In the figures above, we can observe different examples of a controlled monodisperse stream jet. In figure 3.4, all jets were obtained using the same fluid (jet fuel and biofuel mixture) and the same pinhole size ($150\ \mu m$) with different flow rates, while, in figure 3.5, all jets were acquired using the same flow rate ($3.5\ ml/min$) and the same pinhole size ($100\ \mu m$) for different fluids.

For figure 3.4, it is possible to observe that the continuous jet length grows when the inlet

flow rate is increased, while the droplets diameter appears to decrease when higher flow rates are applied. As expected, this corresponds to the same conclusions as the ones obtained for figure 3.1, since both figures compare the variation of different flow rates, using the same conditions (pinhole size and fluid). However, the two figures differ in the working regime, showing that flow rate variation has the same influence for the monodisperse regime as it has for the free liquid jet regime.

In figure 3.5, we can observe that it was possible to reach the present regime using all three fluids. In the previous work [31], water was the only fluid tested, so it was important to understand if we could reach this regime with jet fuel and the jet fuel and biofuel mixture, since both of them have much lower surface tension than water [36]. Also, it is possible to observe that the continuous length for the jet fuel case is much larger than for the other two fluids. The difference between jet fuel and water can be explained by the difference of their surface tension values, since the Rayleigh jet breakup is caused by the growth of asymmetric oscillation of the jet surface, induced by the surface tension. Water surface tension is almost three times higher than jet fuel, allowing the jet to break up earlier, consequently generating a smaller continuous jet length. The same logic would be applied to the jet fuel and biofuel mixture because its surface tension is almost the same as the jet fuel. However, it is possible to observe that the jet fuel and biofuel mixture continuous jet length has roughly the same length as water. This can be explained with the differences between these two fluids viscosity. The mixture has much higher viscosity than jet fuel and water [36], hence it is not possible to apply the same logic to compare them, since it is necessary to consider the fluids viscosity, in contrast to what was stated before. Weber [7] extended Rayleigh theory to include viscous liquids and with his work, it was possible to conclude that viscosity dampens the instability, reducing the continuous length for viscous liquids, explaining the continuous lenght difference between jet fuel and the mixture of jet fuel and biofuel. Then, it is possible to conclude that the mixture cannot be treated as an inviscid liquid in this analysis.

In order to fully characterise the droplet generator, it is necessary to identify for which conditions this regime can be obtained. In order to achieve that, the data was organised in the tables 3.1, 3.2, and 3.3, one for each fluid, where the symbol MD represents the monodispersity phenomenon and displays in the tables for what property values monodispersity can be found. The flow rate and frequency values presented in the tables correspond to the ones used to in the experimental tests and their variation depends on those tests. For example, different flow rates were used for each pinhole because nozzles with larger diameter need a higher flow rate in order to generate a monodisperse stream jet while, for the smaller pinhole, a flow rate of $1.5\ ml/min$ already generates monodisperse droplets. As stated in chapter 2.3, the first monodisperse regime to be found for each case was the starting point and, since this is the lowest flow rate to generate monodispersity, it was decided to study more three higher flow rate values with a variation of $1\ ml/min$ between them, resulting in a different range of flow rate values for each case. Nevertheless, this did not compromise the visualisation analysis since every case has more than one flow rate value in common.

Some of the cases in the tables are marked with an MD*. In contrast to the cases marked with MD, the cases marked with a MD* do not represent monodispersity for only one frequency, they represent a range of frequencies in the neighborhood of the frequency marked on the tables. Looking at table 3.1 it is possible to observe one of the cases with a different symbol (MD*), that corresponds to a pinhole size of $200\ \mu m$ and a flow rate of $3.5\ ml/min$, where the monodisperse regime is identified only for one frequency ($2\ kHz$). However, a lower of frequencies were tested with the objective of trying to identify a range of values for this case and monodispersity was found between $1.5\ kHz$ and $2\ kHz$.

As previously explained for table 3.1, table 3.2 also has some of the monodisperse cases marked with MD*. For these cases, a larger range of frequencies were observed but they are not represented in the table. For this table in particular, all of them can be found in the pinhole $200\ \mu m$ section. The range of frequencies found for the first flow rate ($2.5\ ml/min$) was $1\ kHz$ to $1.4\ kHz$, while the range of frequencies found for the second flow rate ($3.5\ ml/min$) was between $2\ kHz$ to $2.5\ kHz$. For the third flow rate ($4.5\ ml/min$), the range of frequencies found was from $2.5\ kHz$ to $3\ kHz$ and for the last flow rate ($5.5\ ml/min$), the range of frequencies found was $3\ kHz$ to $3.5\ kHz$.

Similar to the other tables, it is possible to observe cases marked with MD* in table 3.3. For the case that corresponds to a pinhole size of $200\ \mu m$ and a flow rate of $3.5\ ml/min$, the frequency range found was $1\ kHz$ to $1.2\ kHz$ and for the case that corresponds to a pinhole size of $200\ \mu m$ and a flow rate of $5.5\ ml/min$, the frequency range found was $2.7\ kHz$ to $3.3\ kHz$.

All particular cases explained for each table were only found for experiments with a pinhole size of $200\ \mu m$, since a smaller number of frequencies were found for these regimes and the droplet diameter variation is more sensible to frequency variations. So it was decided to vary the frequency in smaller magnitude in order to get a range of frequencies for all cases, allowing to study the difference of droplet diameter for each case.

Analysing all tables, it is possible to conclude that, with a smaller pinhole, a larger range of frequencies enables the device to work in the monodisperse regime, and it is necessary to employ higher frequencies for a smaller pinhole compared to a higher one, when working with the same flow rate. This can be explained by the wave number, detailed in section 1.2.4. All devices that produce monodisperse droplets have a working range of frequencies that can be specified by a suitable range of wave numbers, as seen in equation 1.10. This range is the same for different flow rates and different pinhole sizes, meaning that when the droplet diameter has an higher value (result of a bigger pinhole), a lower range of frequency values would produce monodisperse droplets. The reverse logic can be applied to the second conclusion, if the pinhole is smaller, the droplet diameter is smaller and a higher frequency is needed in order to obtain the devices wave number range.

Table 3.1: Monodisperse regimes identification using water.

Pinhole 200μm		**Frequency (kHz)**										
		2	**3**	**4**	**5**	**6**	**7**	**8**	**9**	**10**	**11**	**12**
Flow rate (ml/min)	**3.5**	MD*	-	-	-	-	-	-	-	-	-	-
	4.5	MD	MD	-	-	-	-	-	-	-	-	-
	5.5	-	MD	MD	-	-	-	-	-	-	-	-
	6.5	-	-	MD	MD	-	-	-	-	-	-	-
Pinhole 150 μm		**Frequency (kHz)**										
		2	**3**	**4**	**5**	**6**	**7**	**8**	**9**	**10**	**11**	**12**
Flow rate (ml/min)	**2.5**	-	MD	MD	-	-	-	-	-	-	-	-
	3.5	-	-	-	MD	MD	MD	MD	-	-	-	-
	4.5	-	-	-	MD	MD	MD	MD	MD	-	-	-
	5.5	-	-	-	-	-	MD	MD	MD	MD	MD	MD
Pinhole 100μm		**Frequency (kHz)**										
		2	**3**	**4**	**5**	**6**	**7**	**8**	**9**	**10**	**11**	**12**
Flow rate (ml/min)	**1.5**	-	-	-	MD	MD	MD	-	-	-	-	-
	2.5	-	-	-	-	MD	MD	MD	MD	MD	MD	MD
	3.5	-	-	-	-	-	-	-	MD	MD	MD	MD
	4.5	-	-	-	-	-	-	-	-	-	-	-
Pinhole 100 μm		**Frequency (kHz)**										
		13	**14**	**15**	**16**	**17**	**18**	**19**	**20**	**21**	**22**	**23**
Flow rate (ml/min)	**1.5**	-	-	-	-	-	-	-	-	-	-	-
	2.5	MD	-	-	-	-	-	-	-	-	-	-
	3.5	MD	MD	-	-	-	-	-	-	-	-	-
	4.5	-	-	MD	MD	MD	MD	MD	MD	MD	MD	MD

Table 3.2: Monodisperse regimes identification using jet fuel.

Pinhole 200 μm		**Frequency (kHz)**										
		1	**2**	**3**	**4**	**5**	**6**	**7**	**8**	**9**	**10**	**11**
Flow rate (ml/min)	**2.5**	MD*	-	-	-	-	-	-	-	-	-	-
	3.5	-	MD*	-	-	-	-	-	-	-	-	-
	4.5	-	-	MD*	-	-	-	-	-	-	-	-
	5.5	-	-	MD*	-	-	-	-	-	-	-	-
Pinhole 150 μm		**Frequency (kHz)**										
		1	**2**	**3**	**4**	**5**	**6**	**7**	**8**	**9**	**10**	**11**
Flow rate (ml/min)	**2.5**	-	MD	MD	MD	-	-	-	-	-	-	-
	3.5	-	-	-	MD	MD	MD	MD	-	-	-	-
	4.5	-	-	-	-	MD	MD	MD	MD	MD	-	-
	5.5	-	-	-	-	-	-	MD	MD	MD	MD	MD
Pinhole 100 μm		**Frequency (kHz)**										
		5	**6**	**7**	**8**	**9**	**10**	**11**	**12**	**13**	**14**	**15**
Flow rate (ml/min)	**1.5**	MD	MD	MD	MD	MD	-	-	-	-	-	-
	2.5	-	-	-	-	-	MD	MD	MD	MD	MD	MD
	3.5	-	-	-	-	-	-	-	-	-	-	MD
	4.5	-	-	-	-	-	-	-	-	-	-	-
Pinhole 100 μm		**Frequency (kHz)**										
		16	**17**	**18**	**19**	**20**	**21**	**22**	**23**	**24**	**25**	**26**
Flow rate (ml/min)	**1.5**	-	-	-	-	-	-	-	-	-	-	-
	2.5	MD	MD	MD	-	-	-	-	-	-	-	-
	3.5	MD	MD	MD	MD	MD	MD	MD	-	-	-	-
	4.5	-	-	-	MD	MD	MD	MD	MD	MD	MD	MD

Table 3.3: Monodisperse regimes identification using a jet fuel and biofuel mixture.

Pinhole 200 μm		**Frequency (kHz)**										
		1	**2**	**3**	**4**	**5**	**6**	**7**	**8**	**9**	**10**	**11**
Flow rate (ml/min)	**3.5**	MD*	-	-	-	-	-	-	-	-	-	-
	4.5	-	MD	-	-	-	-	-	-	-	-	-
	5.5	-	-	MD*	-	-	-	-	-	-	-	-
	6.5	-	-	-	MD	-	-	-	-	-	-	-
Pinhole 150 μm		**Frequency (kHz)**										
		1	**2**	**3**	**4**	**5**	**6**	**7**	**8**	**9**	**10**	**11**
Flow rate (ml/min)	**2.5**	MD	-	-	-	-	-	-	-	-	-	-
	3.5	-	-	-	-	MD	MD	MD	-	-	-	-
	4.5	-	-	-	-	-	MD	MD	MD	MD	MD	-
	5.5	-	-	-	-	-	-	-	-	MD	MD	MD
Pinhole 100 μm		**Frequency (kHz)**										
		1	**2**	**3**	**4**	**5**	**6**	**7**	**8**	**9**	**10**	**11**
Flow rate (ml/min)	**1.5**	-	-	MD	MD	-	-	-	-	-	-	-
	2.5	-	-	-	-	-	MD	MD	MD	MD	MD	-
	3.5	-	-	-	-	-	-	-	MD	MD	MD	MD
	4.5	-	-	-	-	-	-	-	-	-	-	-
Pinhole 100 μm		**Frequency (kHz)**										
		12	**13**	**14**	**15**	**16**	**17**	**18**	**19**	**20**	**21**	**22**
Flow rate (ml/min)	**1.5**	-	-	-	-	-	-	-	-	-	-	-
	2.5	-	-	-	-	-	-	-	-	-	-	-
	3.5	MD	MD	MD	-	-	-	-	-	-	-	-
	4.5	MD	MD	MD	MD	MD	MD	MD	-	-	-	-

On the other hand, all pinholes behave in the same way to the flow rate variation: higher flow rate values require higher excitation frequency in order to get the device to work in this regime and it appears that higher flow rates have a larger operation frequency range. This can be explained with the equation 1.10. As seen before, droplet diameter decreases as the flow rate value increases, whereas velocity and Weber number increases, meaning that in order to obtain the same range of wave numbers, a higher frequency needs to be applied to the system. We can use this equation to justify the second conclusion: a higher flow rate generates smaller and faster droplets, allowing a higher range of frequency to fall into the wave numbers range.

All three fluids have similar behaviour through the variation of conditions described previously. However, they have different working conditions, being clear that jet fuel needs higher frequencies in order to enter the monodisperse regime than water and jet fuel and biofuel mixture. This can be explained by analysing the fluid thermophysical properties and equation 1.10. When compared to water, jet fuel has a much smaller surface tension value, requiring higher frequencies to obtain the same wave number range. Analysing these tables taking only into account Rayleigh analysis [5] one would expected that the mixture of jet fuel and biofuel would have similar frequency values to the jet fuel values, due to its surface tension value being similar to the jet fuel surface tension value. As stated before, the mixture has much higher viscosity than jet fuel itself, and Weber [7] theory for viscous liquids needs to be taken into account in order to understand this phenomenon, therefore equation 1.10 is no longer applicable to this situation. Since viscosity dampens the instability, it is to be expected that a lower frequency can generate a monodisperse stream jet, validating the results obtained for the jet fuel and biofuel mixture cases.

3.1.4 Sinuous Wave Breakup

A particular case was found during the experiments and it can be observed in figure 3.6, that shows a sequence of liquid jets that represents the transition between modes of disintegration. This phenomenon was identified by Haenlein [8] and it is characterised by a drop formation due to the waviness of the jet. The aerodynamic forces are now more relevant in the droplet breakup process, while the surface tension is less relevant. This can be explained with the high velocity value used in these tests, resulting in a higher Reynolds number and the type of jet disintegration transitioned from a Rayleigh breakup (figure 3.6a) to a sinuous wave break up (figure 3.6e). The cases presented were the only ones where this regime was found in all processed images and this can be explained by the working conditions: small nozzle, relatively high flow rate and fluid properties that lead to a high velocity jet, entering in a new disintegration mode.

One wonders why this phenomena was not visualised to the case where the previous conditions were used (nozzle size and fluid properties) with a even higher flow rate ($4.5\ min/ml$) than the one presented before ($3.5\ ml/min$), resulting in even higher Reynolds number. We suspect that the phenomena did not appear in this situation because we entered in a transi-

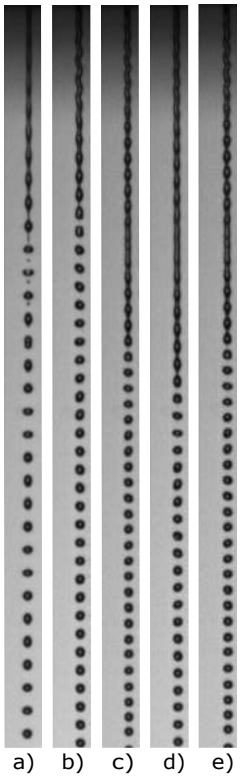

Figure 3.6: Transition between modes of disintegration using jet fuel, a pinhole size of $100\ \mu m$ and a constant flow rate of $3.5\ ml/min$ for different frequencies: a) 18 kHz; b) 19 kHz; c) 20 kHz; d) 21 kHz; e) 22 kHz.

tion portion between the two disintegration modes, where the jet disintegration behaviour is unstable and hard to predict. Then, it is expected that, if the flow rate is set even higher for these conditions, this regime will stabilise and the jet disintegration mode would always be the sinuous wave breakup.

3.2 Monodisperse Regime Characterisation

In this section, the experimental data obtained with the experimental tests will be presented and then analysed. After that, the operational regimes jet droplet diameter and for the jet velocity will be issued and discussed. The process of characterising the different jet properties obtained using the droplet generator is an important step for the device further utilisation, giving the user all the necessary information in order to work with the device. All experimental tests were obtained in an environment with a temperature range from $18°C$ to $20°C$. Since this is a small temperature variation, the effects of temperature in the fluids properties were not taken into account in this analysis.

3.2.1 Droplet Diameter and Distance Between Droplets Characterisation

The first parameter to be analysed and characterised is the jet droplet diameter and the processes used to obtain this parameter are presented in section 2.4. Table 3.4 shows the range of diameters obtained for each case of study, where the smaller value correspond to the first

frequency that generated monodispersity in the experimental tests and the higher value correspond to the last studied frequency that generated monodispersity. The different experimental conditions (fluid, pinhole size, and flow rate) allow to obtain different cases with different diameter values. The fluids and pinhole sizes presented in the table correspond to the ones used in the experimental procedure and the flow rate variation follows the approach explained in the section 2.3. By fixing a pinhole size and choosing one fluid, it is possible to observe that the droplet diameter value decreases with an increase in the flow rate, proving the observations made in subsection 3.1.1. This behaviour can be seen for the three different fluids and pinhole sizes, with one exception for a case where a pinhole size of $100\ \mu m$ and the mixture of jet fuel and biofuel were used. In these cases, the smaller value of the droplet diameter is $197\ \mu m$ for both flow rates of $3.5\ ml/min$ and $4.5\ ml/min$. It was expected for the case with the higher flow rate ($4.5\ ml/min$) to have a smaller diameter value, however, one could consider that a threshold value was found here, where, even with higher flow rates, the droplet diameter would not be smaller for the mixture of jet fuel and biofuel, when used with a pinhole of $100\ \mu m$. However, as explained before, both Rayleigh and Tyler suggested a value for the minimum diameter that is possible to obtain for a maximum instability. With this nozzle size, the expected Tyler diameter is $192\ \mu m$ and the Rayleigh expected value is $189\,\mu m$. The droplet diameter value for the referred is $197\,\mu m$, leading to the conclusion that in this case, the threshold was yet not found.

Also, it is quite noticeable that the droplet diameter is smaller for smaller pinhole sizes, confirming the observations made in section 3.1.1. This kind of behaviour was expected, since, in this kind of device, the nozzle size is the most important feature, influencing the droplet diameter in a significant way.

After analysing the influence of the pinhole size and flow rate in the droplet diameter, it only remains to analyse the influence of the different fluids. It is possible to observe that, for the pinholes of $100\ \mu m$ and $200\ \mu m$, water is the fluid that presents higher diameter values and jet fuel (JF) is the fluid with lower diameter values. However, for the pinhole of $150\ \mu m$ the difference between the three fluids are not consistent, since there are some cases where water and the mixture present lower values than jet fuel.

Table 3.4 also presents the values obtained for the distance between droplets (s_d). While analysing the data, it was not possible to conclude anything for the variation of this parameter with the different conditions (pinhole size, flow rate and fluid) due to its inconsistent variation. One can explain this behaviour with the testing phase. In order to simplify the testing process, the variation of flow rate and frequency were chosen to obtain the sufficient amount of tests, enabling the comparison and characterisation for the different properties. It is accurate to say that it was not possible to completely identify the real range of monodispersity for every tested case, since the real monodisperse limit could be found for frequencies of, for example, $4.8\ kHz$ for the case with a pinhole size of $150\ \mu m$ and flow rate of $3.5\ ml/min$ in table 3.3. As the spacing between droplets values are more sensible to the frequency variation than the droplets diameter, these values become inconsistent. However, the droplets diame-

ters values presented are much closer to the real monodisperse range due to a less sensibility to the frequency variation.

Figures 3.7, 3.8, and 3.9, show the variation of the distance between droplets with frequency for the three different fluids, since frequency was the only parameter that affects the distance between droplets in a consistent manner. In order to achieve this, the experimental data was used to obtain the curve of tendency that shows this variation. In figure 3.7, are presented three cases, one for each fluid, obtained using a pinhole size of $100\ \mu m$ and flow rate of $2.5\ ml/min$. It is possible to observe that, for all fluids, the distance between droplets decreases with the increase of frequency. Despite of having different values, all fluids behave in a similar way. Additionally, figure 3.8 also shows three cases, one for each fluid, yet obtained using a pinhole size of $150\ \mu m$ and a flow rate of $4.5\ ml/min$. Similarly to the case with a pinhole size of $100\ \mu m$, in this case, the distance between droplets decreases with the increase of frequency for all three fluids. Lastly, figure 3.9 also presents one curve for each fluid and the experimental data used was obtained with a pinhole size of $200\ \mu m$. The data obtained for water and for the mixture of jet fuel and biofuel corresponds a flow rate of $4.5\ ml/min$ while the jet fuel case corresponds to a flow rate of $3.5\ ml/min$. In is possible to observe that the the distance between droplets decreases with the increase of frequency for all three fluids, just like the previous figures. Then, it is fair to conclude that the distance between droplets decreases with the increase of frequency and this behaviour is regular to all pinhole size and to different fluids.

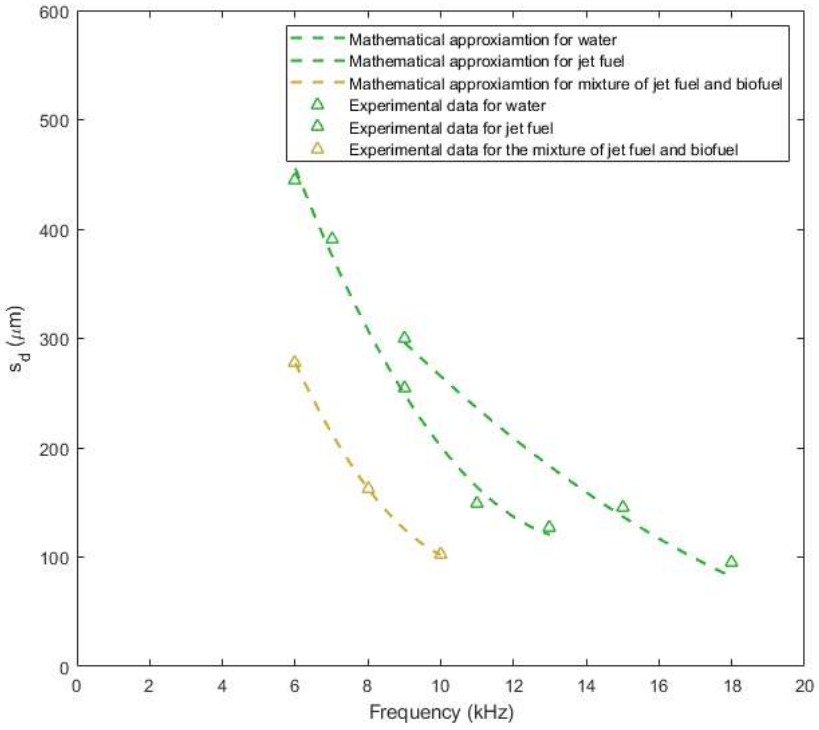

Figure 3.7: Variation of distance between droplets with frequency for a pinhole size of $100\ \mu m$.

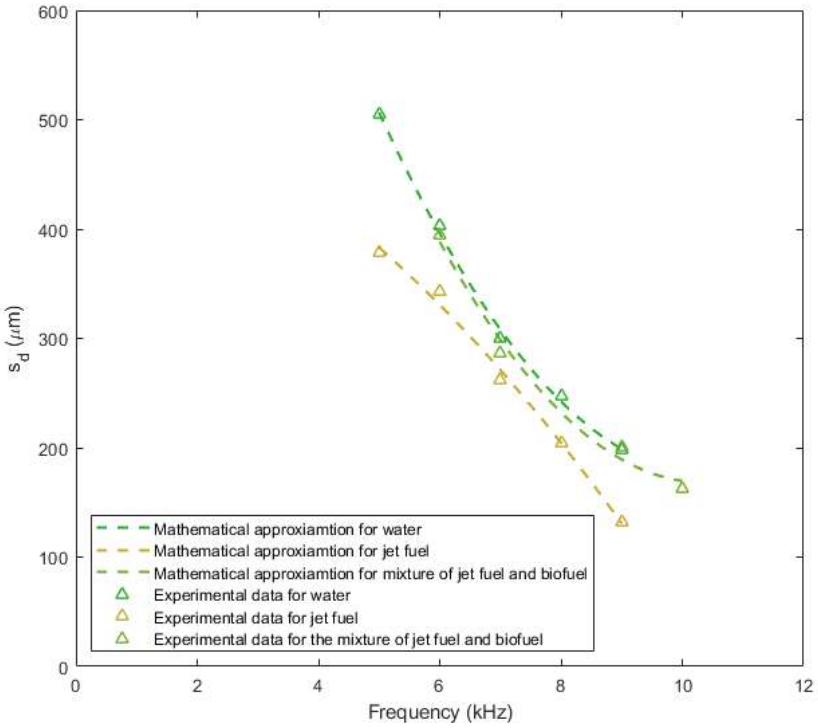

Figure 3.8: Variation of distance between droplets with frequency for a pinhole size of $150\ \mu m$.

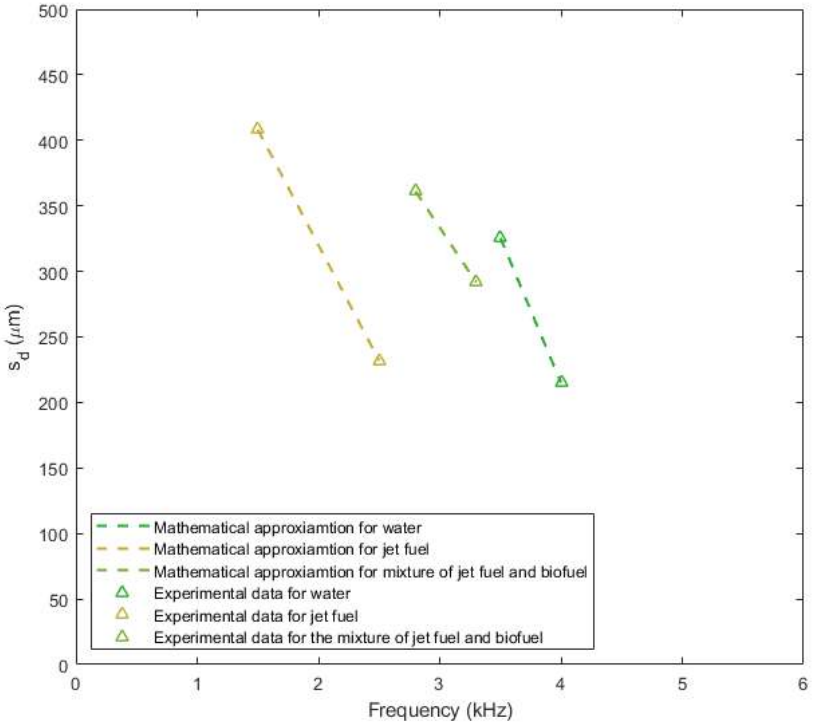

Figure 3.9: Variation of distance between droplets with frequency for a pinhole size of $200\ \mu m$.

Table 3.4: Droplet diameter (D_d) and distance between droplets (s_d) range for tested cases.

Pinhole Size (μm)	**Flow rate (ml/min)**	**H_2O**		**100% JF**		**50% JF/ 50% HVO**	
		D_d [μm]	s_d [μm]	D_d [μm]	s_d [μm]	D_d [μm]	s_d [μm]
200	2.5	-	-	$429 - 472$	$236 - 441$	$464 - 488$	$274 - 387$
	3.5	$453 - 484$	$162 - 328$	$419 - 454$	$232 - 408$	440	363
	4.5	$434 - 457$	$266 - 417$	$400 - 422$	$308 - 449$	$414 - 431$	$292 - 361$
	5.5	$410 - 448$	$204 - 326$	$398 - 409$	$379 - 397$	$393 - 427$	$323 - 491$
	6.5	$401 - 432$	$192 - 318$	–	–	–	–
150	2.5	$318 - 356$	$153 - 347$	$318 - 383$	$196 - 620$	$326 - 340$	$315 - 332$
	3.5	$298 - 338$	$129 - 351$	$297 - 349$	$136 - 406$	$295 - 327$	$186 - 315$
	4.5	$291 - 322$	$198 - 338$	$292 - 339$	$136 - 379$	$288 - 327$	$164 - 394$
	5.5	$290 - 318$	$188 - 313$	$289 - 324$	$154 - 320$	$287 - 314$	$175 - 295$
100	1.5	$242 - 264$	$106 - 224$	$232 - 260$	$106 - 292$	$238 - 258$	$141 - 255$
	2.5	$220 - 251$	$127 - 445$	$204 - 245$	$94 - 300$	$207 - 239$	$102 - 278$
	3.5	$208 - 246$	$146 - 336$	$200 - 225$	$118 - 215$	$197 - 230$	$107 - 309$
	4.5	$206 - 218$	$133 - 199$	$191 - 211$	$124 - 215$	$197 - 215$	$118 - 270$

Table 3.4 shows the data acquired with the experimental testing, giving the information for the tested cases. However, it is necessary to characterise the different conditions that were not tested. To this end, a mathematical approximation was obtained using the experimental data and its tendency, allowing anyone to use the device with the information of which conditions are needed to obtain the required droplet diameter value.

Figure 3.10 presents a mathematical approximation for the droplet diameters to the cases that use a pinhole of $200\ \mu m$ and H_2O. The vertical lines limit the flow rate with the minimum and maximum values studied for this cases, which are $3.5\ ml/min$ for the minimum flow rate tested and $6.5 ml/min$ for the maximum flow rate tested. This case presents a range of diameters of $401\ \mu m - 484\ \mu m$. The curves corresponding to the operational limits of the droplet generator were obtained with a quadratic polynomial regression, using the experimental values, closing the device operation area for this case.

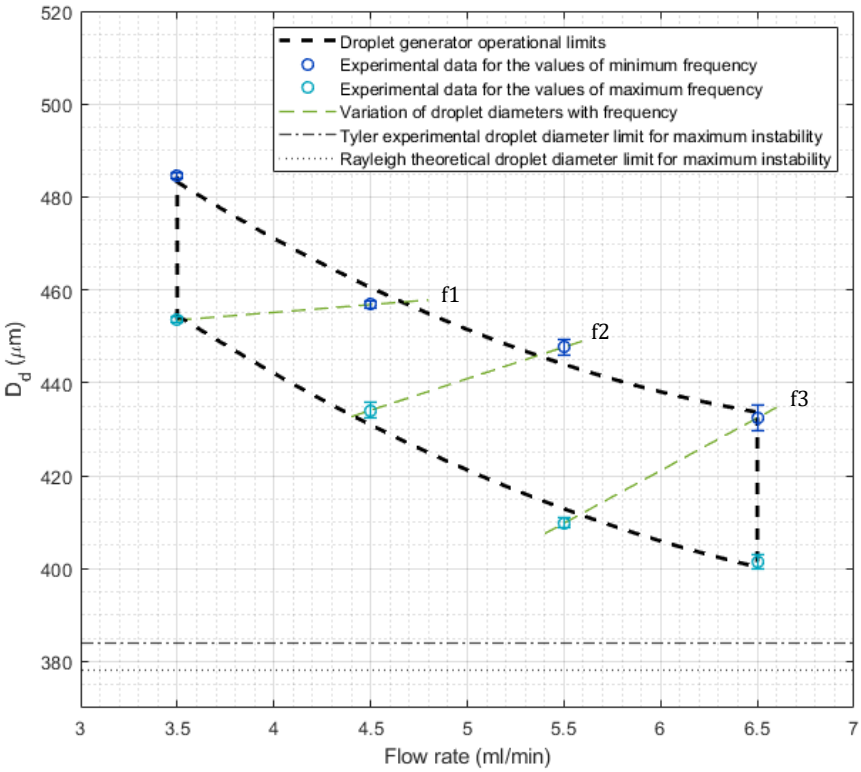

Figure 3.10: Mathematical approximation of the device operational droplet diameters using a pinhole of $200\ \mu m$ and H_2O. Guidelines for different frequencies: $f1 = 2kHz$, $f2 = 3kHz$, $f3 = 4kHz$.

Table 3.5: Frequency values used in the experimental cases shown in figure 3.10.

Flow rate (ml/min)	3.5	4.5	5.5	6.5
Minimum frequency (kHz)	1.5	2.0	3.0	4.0
Maximum frequency (kHz)	2.0	3.0	4.0	5.0

The experimental values and their correspondent uncertainty values obtained with a confidence interval of 95% are represented in the figure and the maximum uncertainty value is

$\pm 2.8\ \mu m$ for the case with a flow rate of $4.5 ml/min$ and frequency of $4\ kHz$. Since the droplet diameter can vary with the flow rate and frequency, a linear approximation was calculated with the values that were obtained with the same frequency and different flow rates, predicting for which values a certain frequency can be used. For a more complete information about droplet diameter variation with frequency, table 3.5 shows the frequency values used to obtain the experimental data presented in figure 3.10. It is also possible to observe the droplet diameter limits expected by Tyler [6] experimental work and Rayleigh [5] theoretical work, which correspond to a droplet diameter value of $384\,\mu m$ and $378\,\mu m$, respectively. The values obtained are distant to these values, leading to the conclusion that the maximum instability condition was not obtained in the testing phase for the present conditions, and that might be achieved with an higher flow rate, being expected that the lower limit could reach one of the mentioned values.

Figure 3.11 shows a mathematical approximation for the droplet diameters to cases that use a pinhole size of $200\ \mu m$ and jet fuel. The droplet generator operation limits were calculated with the same methods explained for figure 3.10, and applied for the data obtained with the present conditions. Yet, for this case, the vertical limits are different from the previous figure, with a minimum flow rate of $2.5\ ml/min$ and a maximum flow rate of $5.5\ ml/min$. With these conditions, it is possible to make droplet diameters between $398\ \mu m$ and $472\ \mu m$ and the maximum uncertainty value is $\pm 3\ \mu m$ for the case with a flow rate of $5.5\,ml/min$ and frequency of $4\ kHz$.

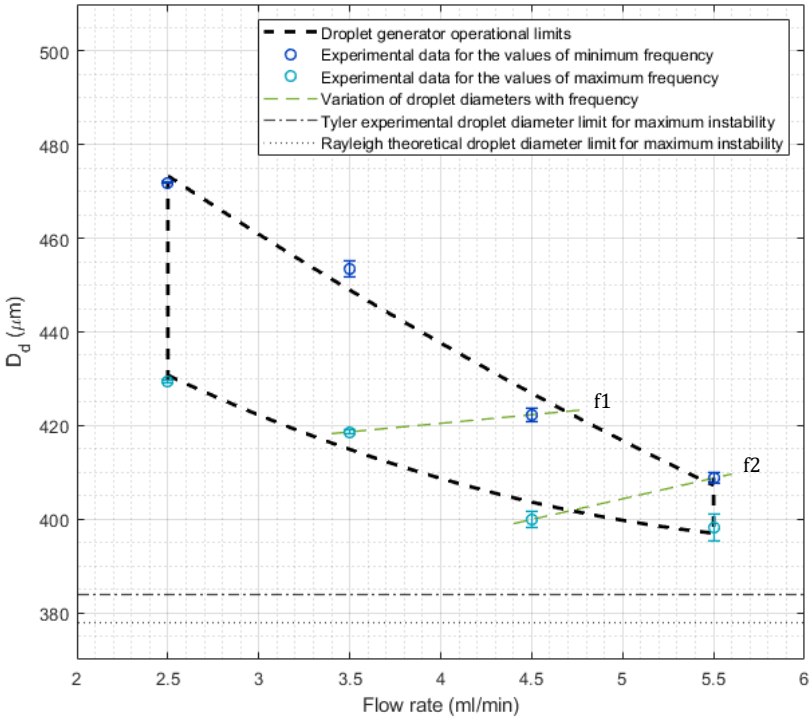

Figure 3.11: Mathematical approximation of the device operation droplet diameters using a pinhole of $200\ \mu m$ and jet fuel. Guidelines for different frequencies: $f1 = 2.5kHz$, $f2 = 3kHz$.

Table 3.6: Frequency values used in the experimental cases shown in figure 3.11.

Flow rate (ml/min)	2.5	3.5	4.5	5.5
Minimum frequency (kHz)	1.0	2.0	2.5	3.0
Maximum frequency (kHz)	1.4	2.5	3.0	3.5

In this figure, a lower number of frequencies is presented when compared with the previous figure, given that only the frequencies of $2.5\ kHz$ and $3\ kHz$ were used for more than one flow rate. Additional information about the frequency used to obtain the experimental data is presented is table 3.6. Similarly to figure 3.10, the experimental values and the mathematical approximation are still distant from the droplet diameter values presented by Tyler and Rayleigh, leading to the conclusion that the maximum instability values were not reached.

Figure 3.12 represents the operational limits for a pinhole size of $200\ \mu m$ and a mixture of jet fuel and biofuel. The droplet generator limits were obtained with the same methods explained for figure 3.10 and 3.11 using the experimental date obtained for this case. The lower diameter value that is possible to obtain with these conditions is $393\ \mu m$ and the higher value is $488\ \mu m$, while the higher uncertainty value with a confidence interval of 95% is $\pm 1.8\ \mu m$ for the case with a flow rate of $4.5\ ml/min$ and a frequency of $2\ kHz$.

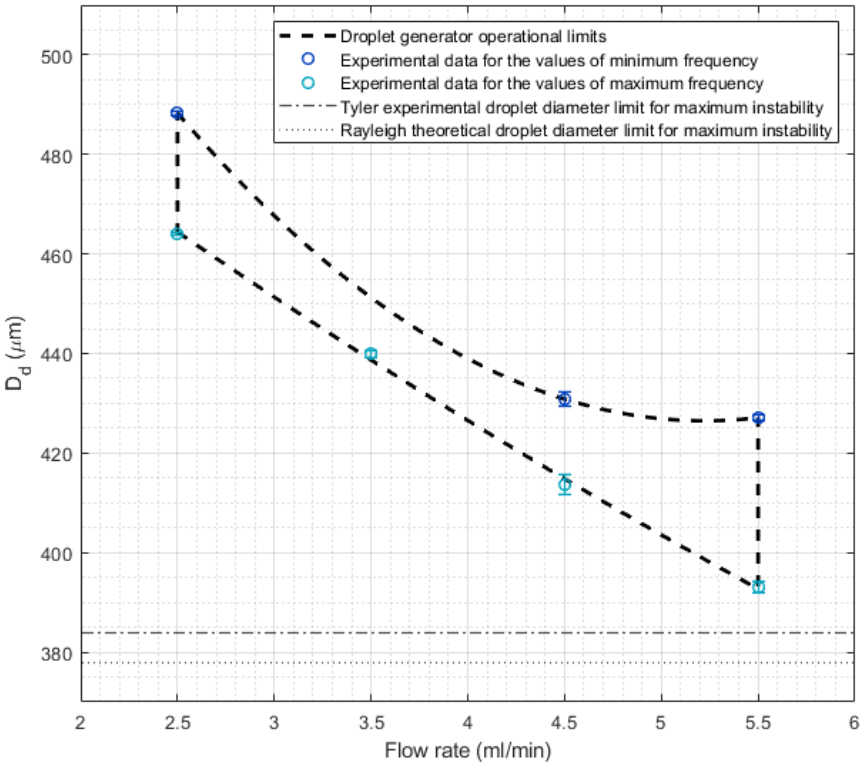

Figure 3.12: Mathematical approximation of the device operation droplet diameters using a pinhole of $200\ \mu m$ and a jet fuel and biofuel mixture.

Table 3.7: Frequency values used in the experimental cases shown in figure 3.12.

Flow rate (ml/min)	2.5	3.5	4.5	5.5
Minimum frequency (kHz)	1.0	–	2.7	3.0
Maximum frequency (kHz)	1.2	2.0	3.3	4.5

For this specific case, in contrast to the previously analysed, it is possible to observe that no frequency lines were calculated, as the frequencies used to obtain the monodisperse regimes were different for each flow rate value and the only frequency information is presented in table 3.7. Similarly to the cases that use a pinhole size of $200\ \mu m$, the experimental data and the mathematical approximation are also far from reach the Rayleigh or Tyler diameter value.

All three areas of operation calculated for the pinhole size of $200\ \mu m$ are different for each fluid and the range of values obtained with each fluid is different as well. However, all three fluids share a range of values from $401 \mu m$ to $472 \mu m$ that can be achieved using all of the them. It is also possible to conclude that it was not possible to reach the maximum instability for none of these cases. This does not compromise the droplet generator operation with this pinhole, only makes the available diameter range smaller.

With the same line of thought, the approximations shown above for a pinhole size of $200\ \mu m$ were also applied for the other two pinhole sizes. Figure 3.13 shows the mathematical approximation for a pinhole size of $150\ \mu m$ and water. The experimental data presented in the figure was used to obtain the operational limits for the present case, that were obtained with the same methods used in the previous figures, resulting in this area of operation, that presents diameter values between $290\ \mu m$ and $356\ \mu m$. The higher uncertainty value for the experimental data was $\pm 2\ \mu m$, for the case with flow rate of $4.5\ ml/min$ and a frequency of $6\ kHz$. For the present case, it was possible to find three frequency lines, marked as $f1$, $f2$ and $f3$. Table 3.8 shows the frequency values used in the experimental tests. It is also possible to observe that the curve obtained with the experimental data for the values of maximum frequency almost reached the diameter value proposed by Tyler and, it is expected that, for even higher flow rates, the droplet diameter would not exceed that value, since it represents the minimum droplet diameter obtained with the maximum instability.

Figure 3.14 shows the mathematical approximation of the device droplet diameters for a pinhole size of $150\ \mu m$ and jet fuel. The range of values possible to obtain with these conditions are $289 \mu m$ to $383 \mu m$. From all the figures that represent the mathematical approximation for the different conditions, this case allowed to obtain the highest number of frequency lines. Altogether, a group of six frequency lines were plotted using the experimental data. Table 3.9 shows the specific frequencies for the values of minimum and maximum frequency. The highest uncertainty value, of $\pm 2.8\ \mu m$, was obtained for a flow rate of $2.5\ ml/min$ and frequency of $2\ kHz$. Similarly to figure 3.13, the droplet generator lower limit almost reached the experimental diameter value obtained by Tyler.

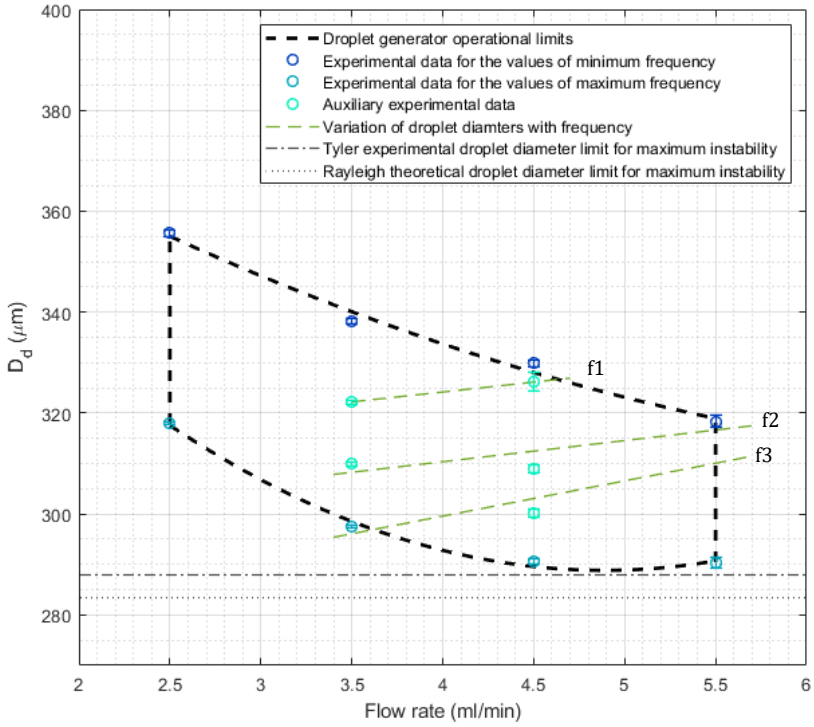

Figure 3.13: Mathematical approximation of the device operation droplet diameters using a pinhole of $150\ \mu m$ and H_2O. Guidelines for different frequencies: $f1 = 6kHz$, $f2 = 7kHz$, $f3 = 8kHz$.

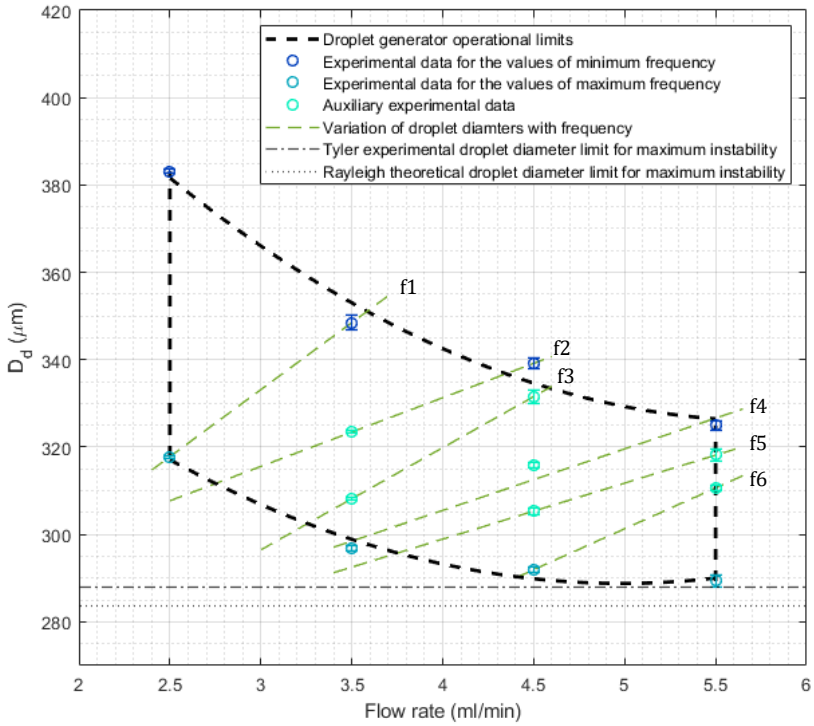

Figure 3.14: Mathematical approximation of the device operation droplet diameters using a pinhole of $150\ \mu m$ and jet fuel. Guidelines for different frequencies: $f1 = 4kHz$, $f2 = 5kHz$, $f3 = 6kHz$, $f4 = 7kHz$, $f5 = 8kHz$, $f6 = 9kHz$.

Table 3.8: Frequency values used in the experimental cases shown in the figure 3.13.

Flow rate (ml/min)	2.5	3.5	4.5	5.5
Minimum frequency (kHz)	3.0	5.0	5.0	7.0
Minimum frequency (kHz)	4.0	8.0	9.0	12.0

Table 3.9: Frequency values used in the experimental cases shown in the figure 3.14.

Flow rate (ml/min)	2.5	3.5	4.5	5.5
Maximum frequency (kHz)	2.0	4.0	5.0	7.0
Minimum frequency (kHz)	4.0	7.0	9.0	11.0

The first noticeable parameters in figure 3.15 are the experimental data errorbars. In general, the uncertainty values for this case appear to be higher than for the other cases. However, these parameters appear to be higher than they actually are, due to a smaller scale for the droplet diameter axis, used for this particular case. The range of values possible to obtain with this conditions are $287\ \mu m$ to $340\ \mu m$ and the highest uncertainty value is $\pm 3.3\ \mu m$ for the case with a flow rate of $5.5\ ml/min$ and frequency of $9\ kHz$.

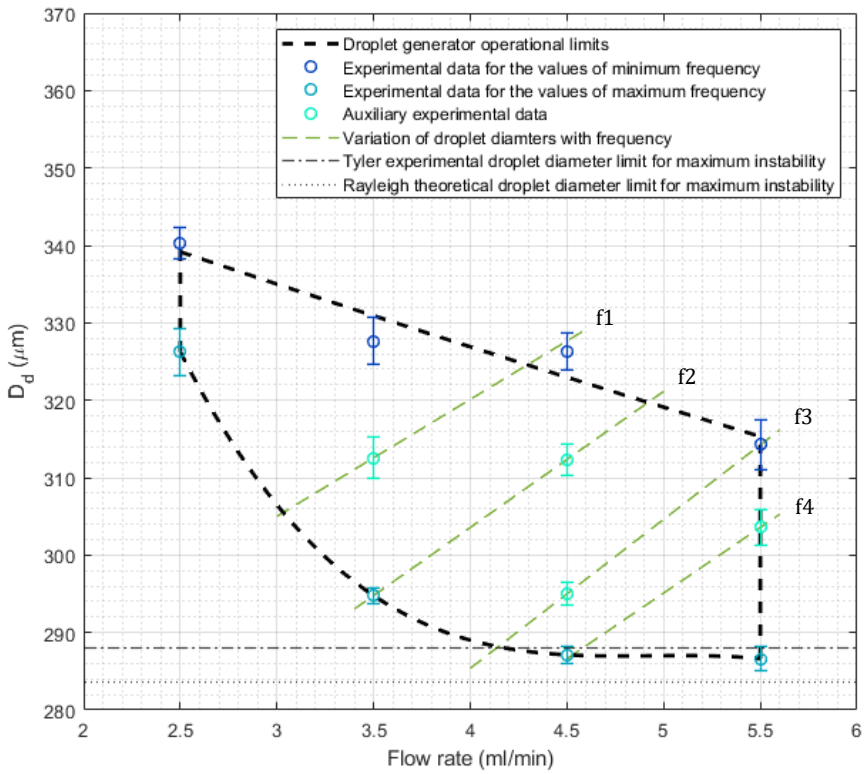

Figure 3.15: Mathematical approximation of the device operation droplet diameters using a pinhole of $150\ \mu m$ and a biofuel and jet fuel. Guidelines for different frequencies: $f1 = 6kHz$, $f2 = 7kHz$, $f3 = 9kHz$, $f4 = 10kHz$.

The lower mathematical limits for this case and two experimental values, exceeded the Tyler experimental diameter value and it seems, even for a higher flow rate, that the curve would

not reach the the Rayleigh theoretical value. Yet, four frequency lines were obtained and table 3.10 shows the frequency values for the experimental data, the minimum and maximum frequency.

Table 3.10: Frequency values used in the experimental cases shown in the figure 3.15.

Flow rate (ml/min)	2.5	3.5	4.5	5.5
Maximum frequency (kHz)	1.0	4.0	5.0	9.0
Minimum frequency (kHz)	2.0	7.0	10.0	12.0

All three areas of operation obtained for the pinhole size of $150\,\mu m$ are different for each fluid and the range of values obtained with each fluid is different as well. However, all three fluids share a range of values from $290\ \mu m$ to $340\ \mu m$ that can be obtained using all of the them. In this case, the experimental data and the mathematical approximation for high flow rates and frequencies reached the diameter value predicted by Tyler for the droplet diameters. It is possible to conclude that it is not possible to lower even more the diameters values than the ones obtained, according to the limits by Tyler. The values obtained in the present work indicate that the diameter value expected by Rayleigh might not be reached in any case.

Finally, the prior analysis is now used for the cases with a pinhole size of $100\ \mu m$ and for the three different fluids. For the case where the fluid used was water, the mathematical approximation of the device operation droplet diameters are presented in figure 3.16. The range of values that is possible to obtain are $206\ \mu m$ to $264\ \mu m$ and the highest uncertainty value is $\pm 2\ \mu m$ for the case with a flow rate of $3.5\ ml/min$ and a frequency of $9\ kHz$ The operation limits follow a similar behaviour to the previous analysis and three frequency lines were obtained that show the droplet diameter variation with the frequency, while the frequencies used to obtained the experimental data are shown in table 3.11. The data obtained for this case are far from the predicted diameter values for the maximum instability.

Figure 3.17 shows the mathematical approximation applied to a pinhole size of $100\,\mu m$, while using jet fuel as fluid. For this case it was possible to calculate four frequency lines and to obtain a range of diameter values from $191\ \mu m$ to $260\ \mu m$. Table 3.12 shows the frequency values used to obtain the experimental monodispersy presented in the figure. Generally, the uncertainty values are lower than $\pm 1\ \mu m$ while the higher value, obtained for the case with a flow rate of $4.5\,ml/min$ and a frequency of $19\,kHz$, was $\pm 2.6\,\mu m$. The figure lower limit reach the experimental value predicted by Tyler and the curve seems to stabilise at that value. It is possible to conclude that for this case, the maximum instability value was reached.

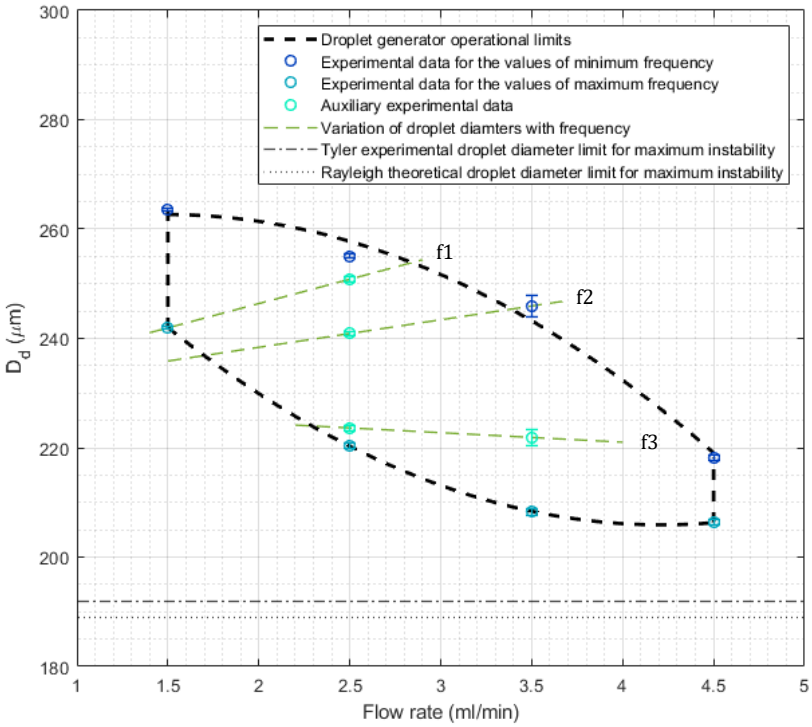

Figure 3.16: Mathematical approximation of the device operation droplet diameters using a pinhole of $100\ \mu m$ and water. Guidelines for different frequencies: $f1 = 7kHz$, $f2 = 9kHz$, $f3 = 11kHz$.

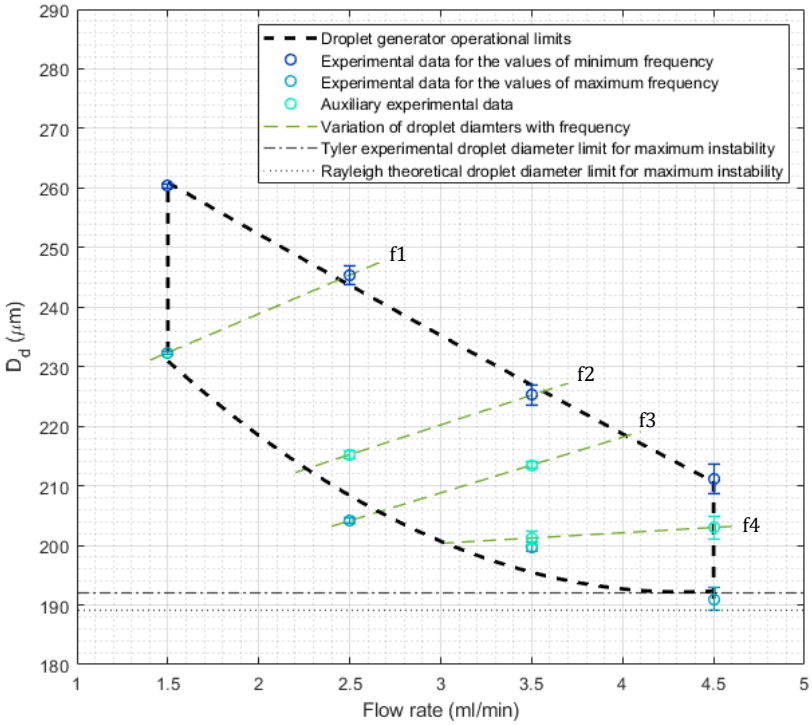

Figure 3.17: Mathematical approximation of the device operation droplet diameters using a pinhole of $100\ \mu m$ and jet fuel. Guidelines for different frequencies: $f1 = 9kHz$, $f2 = 15kHz$, $f3 = 19kHz$, $f4 = 22kHz$.

Table 3.11: Frequency values used in the experimental cases shown in the figure 3.16.

Flow rate (ml/min)	1.5	2.5	3.5	4.5
Maximum frequency (kHz	5.0	6.0	9.0	13.0
Minimum frequency (kHz)	7.0	13.0	14.0	23.0

Table 3.12: Frequency values used in the experimental cases shown in the figure 3.17.

Flow rate (ml/min)	1.5	2.5	3.5	4.5
Maximum frequency (kHz)	5.0	9.0	15.0	19.0
Minimum frequency (kHz)	9.0	18.0	23.0	27.0

Finally, the last mathematical approximation (figure 3.18) was obtained with a pinhole size of $100\,\mu m$ and the jet fuel and biofuel mixture and a range of values between $195\,\mu m$ and $258\,\mu m$ can be obtained in these conditions. Four different frequency lines were obtained using the experimental data shown in the figure that display the diameter variation for different frequencies. Additional information about the frequency used to obtain the experimental data is shown in table 3.13. The experimental data uncertainties are fairly low for this particular case and the highest value, of $\pm 1.5\,\mu m$, was obtained with a flow rate of $1.5\,ml/min$ and a frequency of $3\,kHz$. The figure lower limit did not reach the Tyler or Rayleigh diameter values, meaning that the maximum instability value was not achieved for this case.

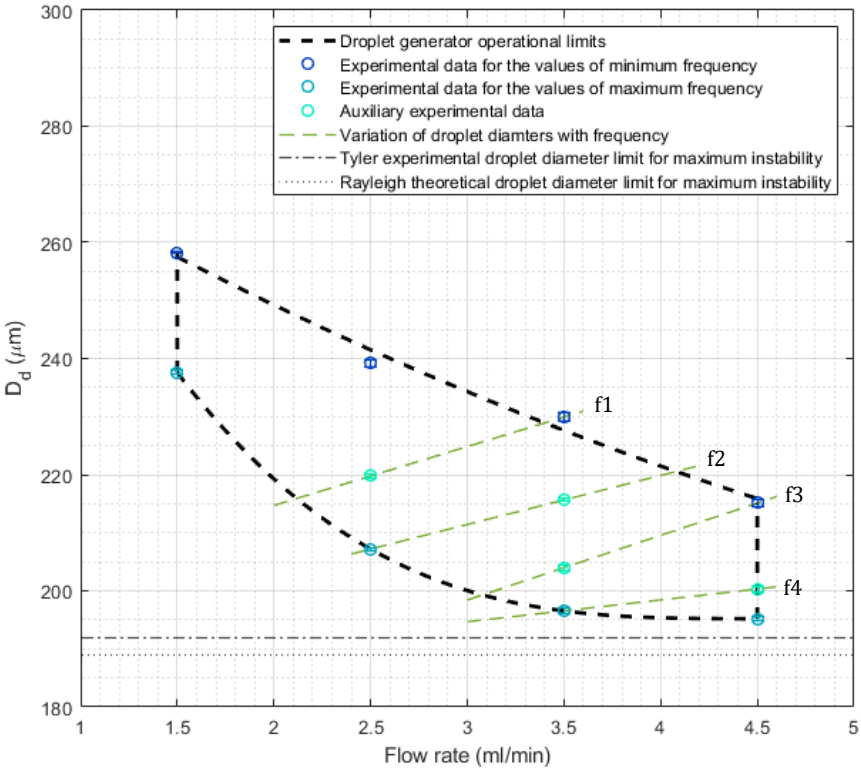

Figure 3.18: Mathematical approximation of the device operation droplet diameters, using a pinhole of $100\,\mu m$ and a biofuel and jet fuel mixture. Guidelines for different frequencies: $f1 = 8kHz$, $f2 = 10kHz$, $f3 = 12kHz$, $f4 = 14kHz$.

Table 3.13: Frequency values used in the experimental cases shown in the figure 3.18.

Flow rate (ml/min)	1.5	2.5	3.5	4.5
Maximum frequency (kHz)	3.0	6.0	8.0	12.0
Minimum frequency (kHz)	4.0	10.0	14.0	18.0

All three areas of operation obtained for the pinhole size of $100\,\mu m$ are different for each fluid and the range of values obtained with each fluid is different as well. However, all three fluids share a range of values from $206\,\mu m$ to $258\,\mu m$ that can be obtained using all of the them. For this case, jet fuel was the only fluid that reached the diameter value predicted by Tyler, while in the water case the values obtained were still far from that value.

A larger range of diameters were obtained for the different cases and the cases that were not achieved with the experimental tests are now fully characterised. It is noticeable that none of the cases reached the value predicted by Rayleigh while some of them reached the experimental value predicted by Tyler. From all pinholes sizes, one could conclude that, the maximum instability was achieved with complete success for the pinhole of $150\ \mu m$.

3.2.2 Jet Velocity Characterisation

Another parameter that needs to be characterised is the jet initial velocity (U_j). The calculation methods for this parameter were explained in subsection 2.4.4.

Table 3.14 shows the velocity values for the experimental tests where three different pinhole sizes, three fluids and four inlet flow rates were used. It is possible to observe that, as expected, the velocity increases with an increase in the flow rate value. A higher flow rate means a higher pressure inside the fluid chamber, leading to a higher emerging jet velocity. When comparing different pinhole sizes, it is possible to conclude that the jet velocity increases for smaller pinhole sizes. This behaviour was expected, given that for the same inlet flow rate, a smaller area would increase the jet emerging velocity. When comparing the three fluids it is possible to observe that, overall, the fluid with higher velocity values was the jet fuel and the fluid that exhibited lower velocity values was the jet fuel and biofuel mixture. The lower velocity values for the mixture can be explained by the role of the viscosity in the jet disintegration process. Viscosity inhibits the growth of instabilities and delay the onset of disintegration, lowering the relative velocity. When comparing the water cases and the jet fuel cases, it is possible to observe that their values are similar for most cases, with the exception for the cases with the pinhole size of $100\ \mu m$.

After organising the experimental data for the jet velocity, it is important to predict the jet velocity for different flow rates using the experimental values. In order to achieve that, a quadratic polynomial regression was obtained using the experimental data, and then plotted, as seen in figures 3.19, 3.20, and 3.21. These figures are divided by pinhole size, and a plot for each fluids and correspondent experimental data is presented. Also, every experimental value has its correspondent uncertainty value, obtained with a confidence interval of 95%.

Table 3.14: Jet Velocity for the tested cases with the variation of pinhole size and flow rate for different fluids.

Pinhole Size (μm)	**Flow rate (ml/min)**	**H_2O**	**100% JF**	**50% JF/ 50% HVO**
		U_j [m/s]	U_j [m/s]	U_j [m/a]
200	2.5	-	0.87	0.80
	3.5	1.29	1.73	1.58
	4.5	2.03	2.15	2.30
	5.5	2.69	2.48	2.90
	6.5	3.10	–	–
150	2.5	2.04	2.00	1.64
	3.5	3.44	3.04	2.64
	4.5	4.11	3.93	3.53
	5.5	4.60	4.52	4.38
100	1.5	2.36	2.72	1.52
	2.5	3.72	5.35	3.12
	3.5	5.29	6.82	4.30
	4.5	6.58	8.18	5.99

Figure 3.19 shows the jet velocity variation with the inlet flow rate and the correspondent experimental data for the pinhole of $200\ \mu m$. We can observe that the mixture is the fluid with the highest velocity and the obtained curve is fairly linear. The jet fuel curve starts to change for flow rates higher than $3.5\ ml/min$. On other hand, overall, water, presents a lower velocity value than the other two curves maintaining the regularity. In fact, it is expected for the obtained curves to be linear, however, these curves were obtained using experimental data, what could lead to a small curvature, shown in the figure. The jet fuel case might be explained by a loss of pressure inside of the liquid chamber, leading to lower values than expected for the experimental cases with flow rates of $4.5\ ml/min$ and $5.5\ ml/min$.

On the other hand, figure 3.20 also represents the jet velocity variation with the inlet flow rate using the experimental data for the pinhole of $150\ \mu m$. In contrast to the jet fuel and biofuel mixture that presents the lower velocity values, water is the fluid with higher velocity values. The mixture and the jet fuel approximations are close to a linear approximation and the water curve has a slight curvature. All three fluids present a similar experimental value for the flow rate value of $5.5\ ml/min$. It is also noticeable that the experimental value for the mixture and a flow rate of $3.5\ ml/min$ has a considerable uncertainty value. Some experimental or measurement errors may have affected this value calculation.

Finally, figure 3.21 presents jet velocity variation with the inlet flow rate and the correspondent experimental data for a pinhole value of $100\ \mu m$. It is possible to notice the difference between the jet fuel values and the other two fluids, given that jet fuel presents much higher velocity values and this behaviour was not noticeable in figures 3.19 and 3.20. This needs to be further studied in order to understand what are the parameters that influence the jet velocity in the different cases.

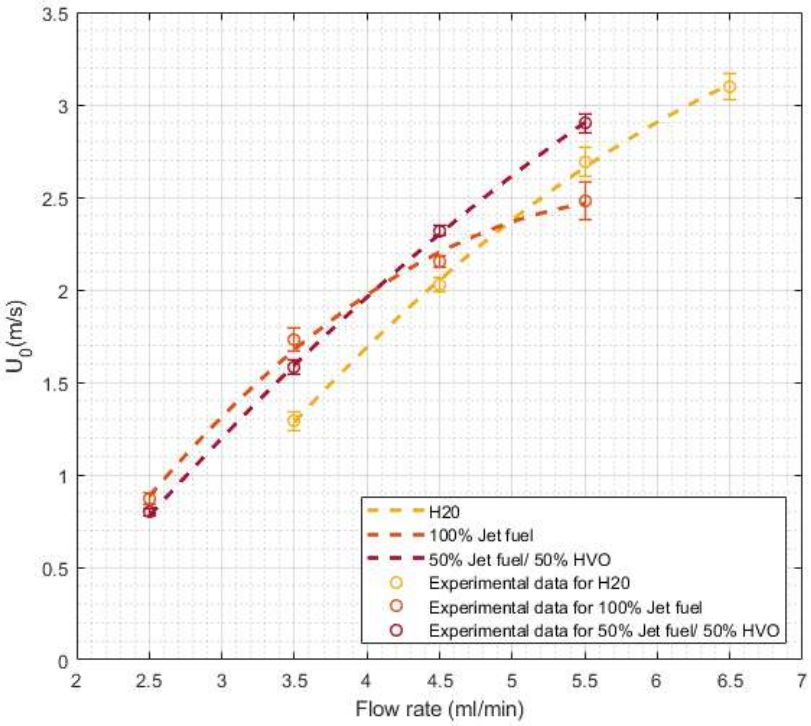

Figure 3.19: Mathematical approximation of the device operational jet velocity for a pinhole size of 200 μm.

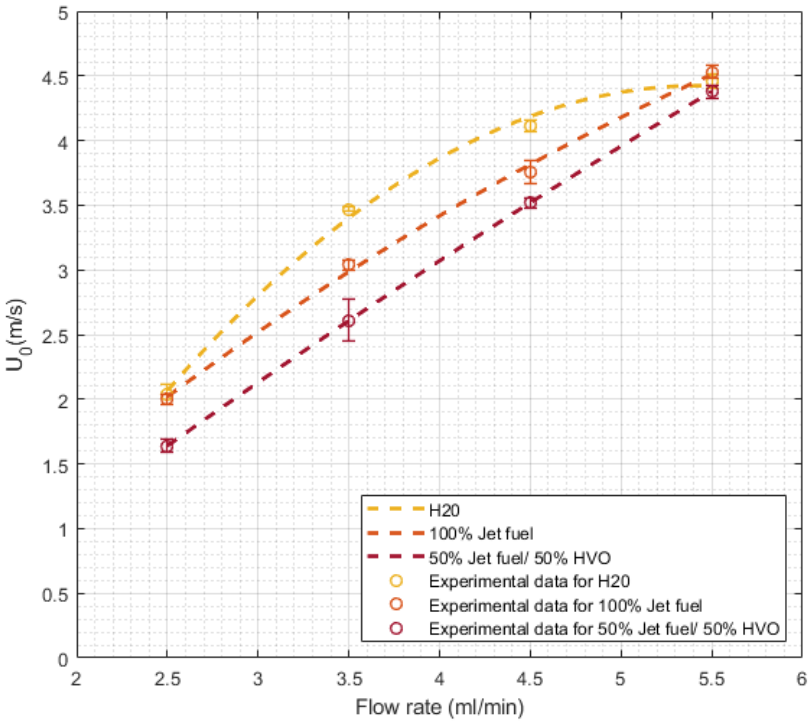

Figure 3.20: Mathematical approximation of the device operational jet velocity for a pinhole size of 150 μm.

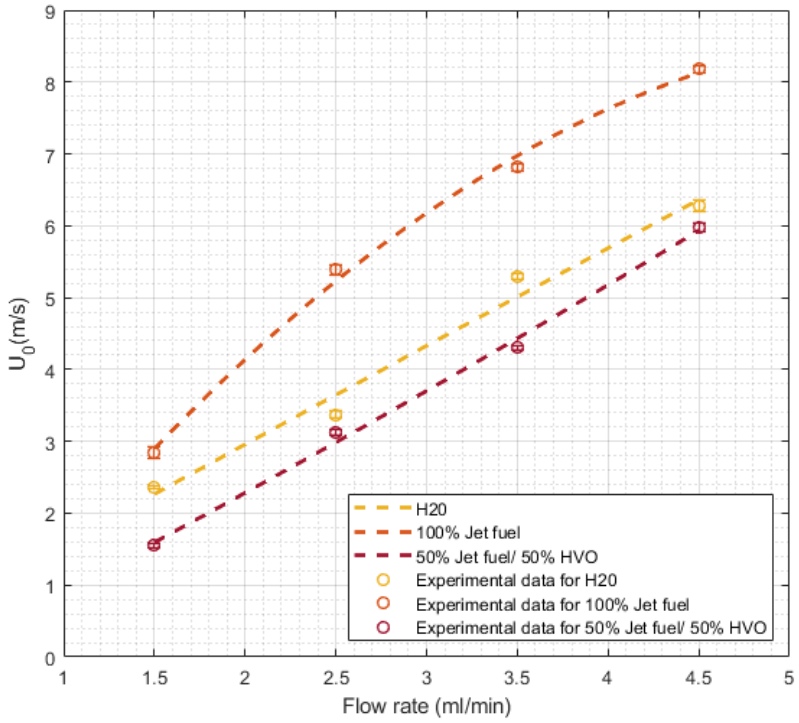

Figure 3.21: Mathematical approximation of the device operational jet velocity for a pinhole size of 100 μm.

3.2.3 Dimensionless Numbers Characterisation

Velocity calculation allowed the determination of three important governing parameters: Reynolds number, Weber number and Ohnesorge number. These parameters were calculated not only for the continuous jet but also for the droplets generated in the monodisperse regime. When calculated for the jet continuous part, the dimensionless numbers can give information about the different regimes and jet behaviour. On the other hand, when calculated for the jet droplets, they present valuable information for the device future utilisation.

Table 3.15 shows the dimensionless numbers applied to the jet continuous part for all tested cases. The first to be analysed is the Reynolds number and it is possible to observe that, for the same fluid and pinhole size, the Reynolds number increases with the increase of the inlet flow rate. The variation in the flow rate changes the jet velocity, while the fluid properties (viscosity and density) and the lenght scale (nozzle diameter) are constant throughout the flow rate variation. After analysing the influence of the flow rate, we can now study the influence of the pinhole size in the Reynolds number. In this case, it is necessary to choose conditions with the same flow rate and fluid for different pinhole sizes. Then, it is possible to understand that, for this case, not only the velocity changes but also the length scale (nozzle diameter). Although, even with a smaller length scale, the Reynolds number still increases due to the resulting higher velocity for smaller pinholes. The last condition that can be analysed is the fluids influence. As expected, the fluid that presents lower Reynolds number is the jet fuel and biofuel mixture and the fluid with higher Reynolds number is water, giving that

the mixture has the highest viscosity and water has the lowest viscosity from all the fluids. It is also possible to observe that, even for the cases where higher velocities were observed for the jet fuel and biofuel mixture, the Reynolds number was not higher than for the other two fluids Reynolds number, leading to the conclusion that the viscous forces have more influence than the inertial forces in the jet formation process. It is also possible to observe that, the Reynolds number values are really low, meaning that all of these cases are working in the laminar regime.

As stated before, the Weber number represents the ratio between the inertial and surface tension forces, being expected that the fluid with lower surface tension would present higher Weber number. This is possible to confirm in table 3.15 comparing water cases with the cases for the other two fluids, where water presents lower values, even for the cases where a higher velocity was observed using water and the same conditions where used (same pinhole size and flow rate) for both fluids. Similarly to the Reynolds number, Weber number also increases with increasing flow rate due to the influence of velocity variation, which is even greater in the Weber number, since in its formula the velocity is squared. The same logic can be applied when analysing the Weber number variation with the pinhole size. Smaller pinhole sizes increase the jet velocity, that increases the Weber number, leading to higher Weber numbers for the cases with smaller pinholes.

The Ohnesorge number is the last dimenssionless number that it is possible to analyse in table 3.15. For the cases that use the same fluid and pinhole size, it is possible to obverse that the Ohnesorge number do not change for different flow rates. As stated previously, this number eliminates the velocity influence, leaving only the fluid properties and the length scale size as the influencing properties that can modify the value. For this case in particular, the properties do not change between cases, leading to an equal Ohnesorge number for all cases. However, when comparing the different fluids for the same pinhole size, it is possible to observe that an higher Ohnesorge number was obtained for the biofuel and jet fuel mixture and lower values were obtained for water. Water presents a lower Ohnesorge number due to an higher surface tension and a lower viscosity. Then, it is possible to conclude that the surface tension forces are predominant in comparison to viscous force for the water cases. The Ohnesorge numbers obtained for the jet fuel cases are higher than the ones obtained for water and lower than the ones obtained for the mixture. This can be explained by the fluid surface tension and viscosity. On one hand, the jet fuel surface tension is almost three times lower than water surface tension. On the other hand, the jet fuel viscosity is lower than the jet fuel and biofuel mixture. It is then possible to conclude that the jet fuel surface tension forces are less predominant than water, yet still more predominant for jet fuel when compared to the mixture. The Ohnesorge number for the jet fuel and biofuel mixture proves what was mentioned earlier in section 3.1.3, this fluid cannot be analysed as an inviscid fluid due the influence of viscosity in the jet formation process.

After determining the jet dimensionless numbers, an interest for the determination of the droplets dimensionless numbers appeared, not only as a comparison between the continu-

ous jet and the droplets properties, but also as a consulting tool for future works that will utilise the droplet generator. Table 3.16 shows the range of the dimensionless numbers obtained for the jet droplets. The dimensionless numbers behave in a similar way to the one explained for table 3.15. However, there are some significant differences: the Reynolds and Weber numbers have higher values for the droplets, due to the length scale used to determine them, the droplet diameter, being at least two times larger than the nozzle size. In contrast to what was observed in table 3.15, the Ohnesorge number varies with the variation of the inlet flow rate. When the Ohnesorge number is obtained for the jet, the jet diameter do not change with the variation of the flow rate. However, for this case, it is possible to obtain different diameter values with the same pinhole by changing the flow rate, leading to different Ohnesorge numbers obtained for the different flow rates.

Table 3.15: Jet dimensionless numbers for each tested case.

Pinhole Size (μm)	**Flow rate (ml/min)**	**H_2O**			**100% JF**			**50% JF/ 50% HVO**		
		Re_j	We_j	$Oh_j \cdot 10^3$	Re_j	We_j	$Oh_j \cdot 10^3$	Re_j	We_j	$Oh_j \cdot 10^3$
200	2.5	–	–	–	123	4.7	17.6	69	3.9	28.6
	3.5	251	4.7	8.4	246	18.8	17.6	140	16.0	28.6
	4.5	404	11.4	8.4	306	29.1	17.6	205	34.5	28.6
	5.5	536	20.1	8.4	354	38.8	17.6	257	54.1	28.6
	6.5	619	26.9	8.4	–	–	–	–	–	–
150	2.5	298	8.7	9.7	214	18.9	20.3	109	12.9	33.1
	3.5	416	16.1	9.7	325	43.6	20.3	173	32.9	33.1
	4.5	616	35.0	9.7	402	66.8	20.3	234	59.7	33.1
	5.5	687	43.9	9.7	484	96.7	20.3	291	92.5	33.1
100	1.5	229	7.7	12.1	203	25.5	24.9	69	7.7	40.5
	2.5	426	26.8	12.1	384	91.3	24.9	138	31.4	40.5
	3.5	514	38.9	12.1	486	146.3	24.9	190	59.3	40.5
	4.5	609	54.6	12.1	583	210.6	24.9	265	115.0	40.5

Table 3.16: Droplets dimensionless numbers for each tested case.

Pinhole Size (μm)	**Flow rate (ml/min)**	**H_2O**			**100% JF**			**50% JF/ 50% HVO**		
		Re_d	We_d	$Oh_d \cdot 10^3$	Re_d	We_d	$Oh_d \cdot 10^3$	Re_d	We_d	$Oh_d \cdot 10^3$
200	2.5	–	–	–	265 – 291	10.1 – 11.1	11.1 – 12.0	161 – 169	9.1 – 9.6	18.3 – 18.8
	3.5	570 – 609	10.6 – 11.3	5.5 – 5.7	516 – 559	39.4 – 42.7	11.7 – 12.2	307	35.1	19.3
	4.5	877 – 923	24.7 – 26.1	5.5 – 5.7	613 – 647	58.1 – 61.4	12.1 – 12.4	424 – 442	71.4 – 74.3	19.5 – 19.9
	5.5	1099 – 1200	41.2 – 45.0	5.6 – 5.8	705 – 724	77.3 – 79.4	12.3 – 12.5	504 – 448	106.2 – 115.4	19.6 – 20.4
	6.5	1242 – 1338	53.7 – 57.8	5.7 – 5.9	–	–	–	–	–	–
150	2.5	631 – 705	18.4 – 20.6	6.4 – 6.8	453 – 546	40.1 – 48.3	12.7 – 14.0	237 – 247	28.2 – 29.4	22.0 – 22.4
	3.5	826 – 939	32.0 – 36.4	6.4 – 6.9	643 – 755	86.3 – 101.3	13.3 – 14.4	341 – 379	64.6 – 71.8	22.4 – 23.6
	4.5	1193 – 1344	68.5 – 77.1	6.5 – 6.9	783 – 909	129.9 – 151.0	13.5 – 14.6	447 – 508	114.2 – 129.8	22.4 – 23.9
	5.5	1339 – 1458	85.7 – 93.3	6.6 – 6.9	934 – 1064	186.6 – 212.6	13.7 – 14.6	556 – 609	176.8 – 193.9	22.9 – 23.9
100	1.5	554 – 604	18.7 – 20.4	7.5 – 7.8	471 – 528	54.2 – 60.7	163 – 177	18.3 – 19.9	25.2 – 26.3	
	2.5	939 – 1069	59.0 – 67.2	7.7 – 8.2	784 – 942	186.4 – 224.0	15.9 – 17.4	286 – 331	65.0 – 75.0	26.2 – 28.1
	3.5	1070 – 1263	81.0 – 95.6	7.7 – 8.4	1018 – 1148	306.4 – 3455	16.2 – 17.2	374 – 437	116.4 – 136.4	26.7 – 28.9
	4.5	1256 – 1329	112.8 – 119.2	8.2 – 8.5	1113 – 1232	402.1 – 444.8	17.1 – 18.0	517 – 569	224.5 – 247.4	27.6 – 29.0

3.3 Analysis of the Behavior of the Jet Continuous Part in a Free Liquid Jet Formation

This chapter presents a brief analysis of the continuous jet length and the influence that the different properties (fluids, flow rate, and pinhole size) have in this parameter. The analysis performed in the visualisation process can now be validated by experimental data and mathematical approximations.

In figure 3.22, it is possible to observe the growth of the continuous jet with with the inlet flow rate for three different fluids (water, jet fuel and a mixture of jet fuel and biofuel), that was obtained with the experimental data shown in the figure. All the experimental data was acquired using a pinhole size of $100\ \mu m$. The first behaviour to notice is the increasing of the continuous jet length with the increase in the flow rate for all cases. This behaviour supports the analysis make in subsection 3.1.1: if the jet diameter is kept constant, the length of the continuous part of the jet is proportional to the jet velocity. It is also quite noticeable that the jet fuel presents higher values for all flow rates than the other two fluids, while water and the mixture have similar values. This was expected since, in the visualisation process, was initially found the differences between the fluids, which are created by the difference in their properties, surface tension and viscosity.

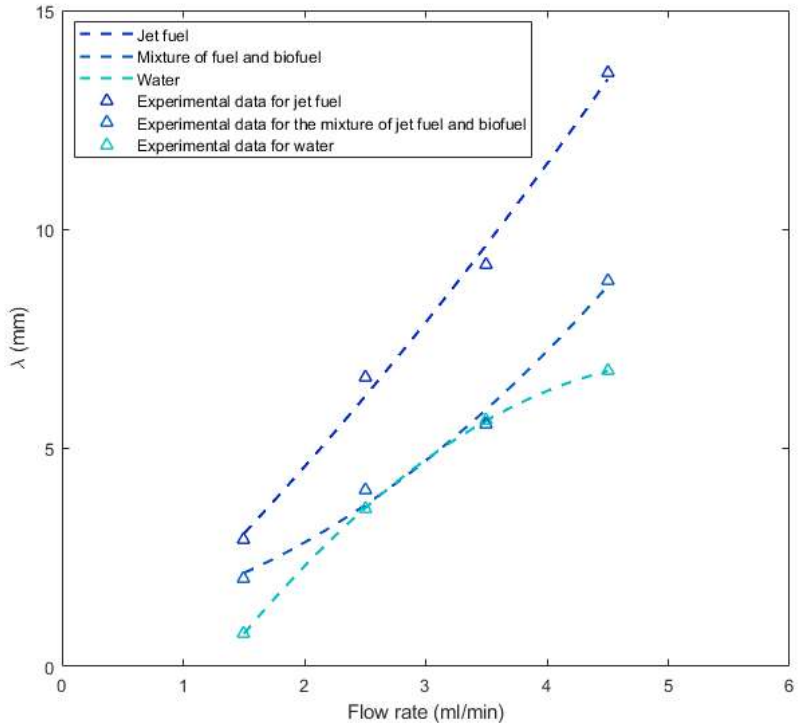

Figure 3.22: Continuous jet lenght growth for three different fluids with a pinhole size of $100\ \mu m$.

Figure 3.23 presents the growth of the continuous jet with the flow rate for each pinhole size while using the same fluid (jet fuel). It is possible to observe that, both pinhole size and jet

velocity (directly proportional to the flow rate) have influence in this parameter. As seen in subsection 3.1.1, Savart theory cannot be applied when both velocity and pinhole size change throughout the analysis. However, it is possible to understand the influence of the velocity in this value. The pinhole size of $200\ \mu m$ presents the lowest continuous jet length of the three pinholes, despite the fact that, for constant jet velocity, this would be the pinhole with the highest values. However, since for the same flow rate, the velocity obtained with this pinhole is lower than with the other two pinholes, the continuous jet length is also smaller. On the other hand, the pinhole of $150\ \mu m$ reaches higher values for small low flow rate than the pinhole of $100\ \mu m$, contradicting the thesis that velocity is more important than pinhole size. In this case, the velocity might not be higher enough for the smaller pinhole to influence the pinhole size factor. On the other hand, when the flow rate is increased, the smaller pinhole reaches higher values than the pinhole of $150\ \mu m$, supporting the thesis that when the velocity is higher enough, becomes the principal factor influencing this parameter.

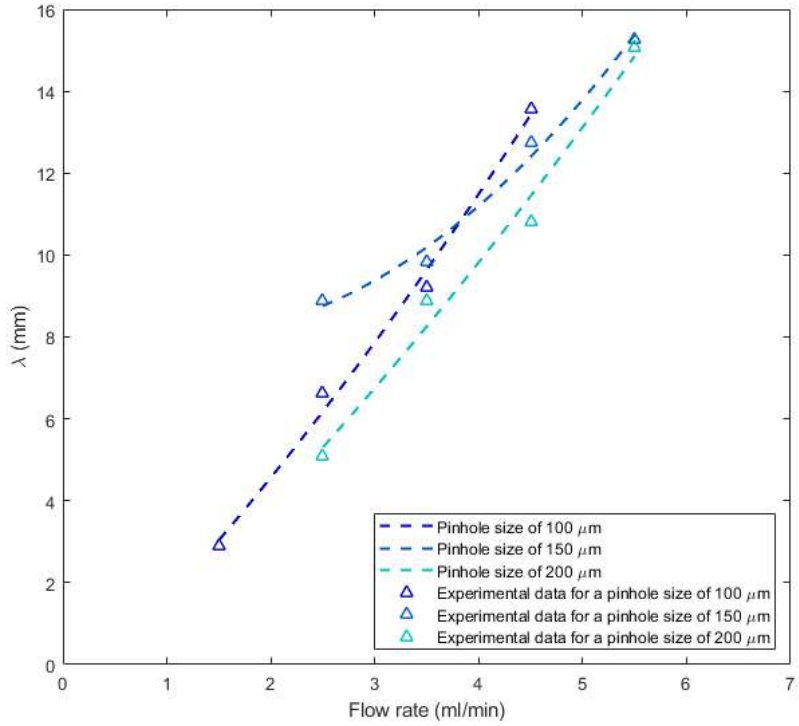

Figure 3.23: Continuous jet lenght growth for three different pinhole sizes using jet fuel as the fluid.

3.4 Summary

In the visualisation process, it was possible to identify the different regimes in the jet formation. The free liquid jet formation allowed to compare the influence of the nozzle size and flow rate in the continuous jet length and droplet diameter. Some cases of secondary droplets were also identified during the experimental testing. All cases of monodispersity were properly identified for the different conditions. The smaller pinhole ($100\ \mu m$) allowed a larger range of frequencies to generate monodisperse regimes while jet fuel needed higher

frequency value in order to enter the monodisperse regime. A different case of jet formation was identified as a sinuous break up, predicted by Haenlein [8].

The characterisation process provided crucial information in order to confirm the conclusions made in the visualisation process. The mathematical approximations obtained for the droplet diameters provided information for the cases that were not experimentally tested. It was observed that the data reached the diameter predicted by Tyler [6] for the cases with a pinhole size of $150\ \mu m$ and all the cases were far from the diameter predicted by Rayleigh [5]. It was noticeable that the jet fuel and biofuel mixture presented some differences when compared with jet fuel and water, what can be explained by the high viscosity that this fluid presents. Given that biofuels are seen as one of the alternatives for the typical aviation jet fuel, it is possible to conclude that due to its properties, some of the processes inside the combustion chamber might be different from the typical jet fuel.

Chapter 4

Conclusions and Future Work

4.1 Conclusions

As stated at the beginning of this dissertation, the present work had two main objectives: the optimisation of a previous droplet generator and the monodisperse regimes characterisation. The droplet generator working principle was maintained and the aspects that needed to be improved were modified in order to optimise the device. Thus, the droplet generator is simpler and easy to use than before and easy to repair.

All the materials used for produce the device are cheap and simple to obtain, leading to the conclusion that it is possible to design and manufacture an affordable droplet generator and obtain jet disintegration for many regimes, conditions and fluids.

It was possible to visualise different phenomena with the droplet generator such as free liquid jet formation, monodisperse jet and satellite droplets. The monodisperse phenomena was analysed with more depth and it was identified for different conditions (flow rate, pinhole size and fluid) due to its importance for the present work and device operation. It was yet observed a sinuous wave, a particular case of a jet formation with the influence of aerodynamic forces.

The pinhole size influence in the jet formation was quite noticeable, specially in the droplet diameter parameter, since it is not possible to generate droplets with diameters smaller than, more or less, two times the nozzle size. All three nozzles generated a large range of diameters and velocities, enabling the user to chose which characteristics the jet should have.

One important step for the device utilisation was the use of three fluids with different characteristics. The droplet generator was able to function for all three fluids, thought, they presented differences in the jet formation process. The fluid properties influenced the process and the biofuel and jet fuel mixture presented distinct behaviour due to its high viscosity. One can conclude that, although the biofuels can be a good option as more efficient ecological solution in the aeronautical sector, it is necessary to consider its differences with the conventional jet fuel.

With the analyses of the behaviour of the jet continuous part in a free liquid jet, it was possible to validate that the continuous jet grows with the increase of the inlet flow rate and the jet fuel case has a much larger continuous jet length than the other two fluids.

Overall, the results obtained and analysed corresponded to what was expected and it can be considered that the present work met the objectives proposed.

4.2 Future Work

The droplet generator characterisation allows anyone to use this device within the tested regimes. Since a large range of droplet sizes and jet velocities were found and characterised, this droplet generator can be used in the future for typical droplet generators applications, such as impact of droplets on solid surfaces or liquid films, droplet evaporation and mechanical droplet-droplet interaction. Other field of application for the droplet generator also include the validation of particles sizing techniques and continuous spray coating.

To some extent, this dissertation is an optimisation of a previous work and more modifications and different analysis can be made, giving continuity to the present work. First, it is suggested the use of smaller pinhole sizes in order to obtain even smaller droplets and higher velocities. Then, the use of more fluids can be interesting for a more extensive characterisation for fluids with different properties. The studies cited previously can improve even further the device working conditions.

Finally, it is suggested to use this device design and try to modify the jet formation process to a drop-on-demand process. This might be interesting given that obtaining the two modes of droplets formation would increase the droplet generator applications. Another possible alteration to the working principle would be charging electrically the droplets and deflect a single droplet from the rest of the stream, which could be interesting in droplet impact studies. Finally, it would also be interesting to study in more depth the sinuous wave breakup found for some of the cases and extend this regime for more cases.

Bibliography

[1] W. van Hoeve, S. Gekle, J. H. Snoeijer, M. Versluis, M. P. Brenner, and D. Lohse, "Breakup of diminutive Rayleigh jets," *Physics of Fluids*, vol. 22, no. 12, 2010.

[2] N. Ashgriz, *"Handbook of atomization and sprays: theory and applications"*. Springer Science & Business Media, 2011.

[3] F. "Savart, *"Ann. Chim. Phys."*, 1833, vol. 53.

[4] J. A. F. Plateau, *"Statique expérimentale et théorique des liquides soumis aux seules forces moléculaires"*. Gauthier-Villars, 1873, vol. 2.

[5] L. Rayleigh, "On the instability of jets," *Proceedings of the London Mathematical Society*, vol. 1, no. 1, pp. 4–13, 1878.

[6] E. Tyler, "Xl. instability of liquid jets," *The London, Edinburgh, and Dublin Philosophical Magazine and Journal of Science*, vol. 16, no. 105, pp. 504–518, 1933.

[7] C. Weber, "Zum Zerfall eines Flüssigkeitsstrahles," *ZAMM – Journal of Applied Mathematics and Mechanics / Zeitschrift für Angewandte Mathematik und Mechanik*, vol. 11, no. 2, pp. 136–154, 1931.

[8] A. Haenlein, *"Desintegration of a Liquid Jet"*. NACA TN 659, 1932.

[9] W. V. Ohnesorge, "Formation of Drops by Nozzles and the Breakup of Liquid Jets," *Applied Mathematics and Mechanics*, vol. 16, pp. 355–358, 1936.

[10] R. D. Reitz, "Atomization and other breakup regimes of a liquid jet," Ph.D. dissertation, Princeton University, 1978.

[11] A. H. Lefebvre and V. G. McDonell, *"Atomization and sprays"*. CRC press, 2017, vol. 2.

[12] P. Walzel, "Koaleszenz von fluüssigkeitsstrahlen an brausen (coalescence of liquid jets at shower-head atomizers)," *Chem.-Ing.-Tech. 52*, pp. 652–654, 1980.

[13] J. M. Schneider and C. D. Hendricks, "Source of uniform-sized liquid droplets," *Review of Scientific Instruments*, vol. 35, no. 10, pp. 1349–1350, 1964.

[14] G. Brenn, T. Helpiö, and F. Durst, "A new apparatus for the production of monodisperse sprays at high flow rates," *Chemical Engineering Science*, vol. 52, no. 2, pp. 237–244, 1997.

[15] N. A. DIMMOCK, “Production of Uniform Droplets,” *Nature*, pp. 686–687, 1950.

[16] N. R. Lindblad and J. M. Schneider, “Production of uniform-sized liquid droplets,” *Journal of Scientific Instruments*, vol. 42, no. 8, pp. 635–638, 1965.

[17] J. Schneider, N. Lindblad, and C. Hendricks, “An apparatus to study the collision and coalescence of liquid aerosols,” *Journal of Colloid Science*, vol. 20, no. 6, pp. 610–616, 1965.

[18] R. N. Berglund and B. Y. Liu, “Generation of Monodisperse Aerosol Standards,” *Environmental Science and Technology*, vol. 7, no. 2, pp. 147–153, 1973.

[19] A. Frohn, N. Roth, and B. Y. H. Liu, *”Dynamics of droplets”*. Springer, 2000, pp. 65–80.

[20] E. K. Dabora, “Production of monodisperse sprays,” *Review of Scientific Instruments*, vol. 38, no. 4, pp. 502–506, 1967.

[21] Y. Hong, N. Ashgriz, and J. Andrews, “Experimental study of bubble dynamics on a micro heater induced by pulse heating,” *Journal of Heat Transfer*, vol. 126, no. 2, pp. 259–271, 2004.

[22] J. R. Castrejón-Pita, G. D. Martin, S. D. Hoath, and I. M. Hutchings, “A simple large-scale droplet generator for studies of inkjet printing,” *Review of Scientific Instruments*, vol. 79, no. 7, 2008.

[23] W. D. Wu, S. X. Lin, and X. D. Chen, “Monodisperse droplet formation through a continuous jet break-up using glass nozzles operated with piezoelectric pulsation,” *AIChE Journal*, vol. 57, no. 6, pp. 1386–1392, 2011.

[24] J. F. Edd, M. Toner, D. Dicarlo, and D. Irimia, “Microfluidic droplet encapsulation,” Jun. 30 2015, uS Patent 9,068,181.

[25] N. Ashgriz, *”Handbook of atomization and sprays: theory and applications”*. Springer Science & Business Media, 2011.

[26] Hue P. Le, “Progress and Trends in Ink-jet Printing Technology,” *Journal of Imaging Science and Technology*, vol. 42, no. 1, pp. 49–62, 1998.

[27] D. A. Wang and N. Z. Liu, “A shear mode piezoelectric energy harvester based on a pressurized water flow,” *Sensors and Actuators, A: Physical*, vol. 167, no. 2, pp. 449–458, 2011.

[28] H. Ulmke, T. Wriedt, and K. Bauckhage, “Piezoelectric droplet generator for the cali-

bration of particle-sizing instruments," *Chemical Engineering and Technology*, vol. 24, no. 3, pp. 265–268, 2001.

[29] T. Laurell, L. Wallman, and J. Nilsson, "Design and development of a silicon microfabricated flow-through dispenser for on-line picolitre sample handling," *Journal of Micromechanics and Microengineering*, vol. 9, no. 4, pp. 369–376, 1999.

[30] K. C. Fan, J. Y. Chen, C. H. Wang, and W. C. Pan, "Development of a drop-on-demand droplet generator for one-drop-fill technology," *Sensors and Actuators, A: Physical*, vol. 147, no. 2, pp. 649–655, 2008.

[31] C. Moura, "Design of a monosized droplet generator," Master Dissertation, Universidade da Beira Interior, 2019.

[32] J. M. Raquez, Y. Habibi, M. Murariu, and P. Dubois, "Polylactide (PLA)-based nanocomposites," *Progress in Polymer Science*, vol. 38, no. 10-11, pp. 1504–1542, 2013.

[33] FILATECH, "Filaflexible-40," https://www.fila-tech.com/product-special/fila-flexible-40, 2020, last accessed 2020-12-16.

[34] "STEMINC", "Diaphragm 3 electrodes self drive 1.8 khz," https://www.steminc.com/PZT/en/piezo-diaphragm-self-drive-1-8k-hz, 2021, last accessed 2021-01-06.

[35] "Standard specification for aviation turbine fuel containing synthesized hydrocarbons," ASTM International, West Conshohocken, PA, Tech. Rep., 2020.

[36] D. Ribeiro, "Experimental study of a single droplet impinging upon liquid films: Jet fuel and biofuel mixtures," Master Dissertation, Universidade da Beira Interior, 2018.

Appendix A

A.1 Properties of the Printable Materials

Table A.1: 3D printable material properties (PLA)

Recommended Print Settings	
Nozzle Temperature [°C]	210
Heatbed Temperature [°C]	40 – 60
Material properties	
Melt temperature [°C]	145 – 160
Specific Gravity [g/cm3]	1.24
Moistore absorbtion factor	0.3
Glass Transition Temperature [°C]	55 – 60

Table A.2: 3D printable material properties (Filaflexible-40)

Recommended Print Settings	
Nozzle Temperature [°C]	220 – 240
Heatbed Temperature [°C]	50 – 60
Material properties	
Melt temperature [°C]	160
Specific Gravity [g/cm3]	1.22
Moistore absorbtion factor	0.2
Glass Transition Temperature [°C]	50